# Residual Seismic Performance of Fire-Damaged Reinforced Concrete Frame Structure with Metallic Yielding Dampers

Ying-Qi Jia[1]; Chao Wang[2]; Ling-Zhi Li[3]; Rui-Fu Zhang[4]; and Zhou-Dao Lu[5]

**Abstract:** Structures with varying dampers have been widely designed and constructed for earthquake resistance. However, the residual seismic performance of these damped structures could not be guaranteed after being exposed to a fire because both the primary structure and dampers are vulnerable to high temperatures. The postfire residual seismic performance is an important design index for damped structures whereas no research has been done so far to determine such residual performance. Therefore, this study serves as the first attempt by exploiting the widely constructed RC frame structure with commonly investigated metallic yielding dampers (MYDs) as an example to investigate its residual seismic performance after being exposed to a fire. One story of a RC office building is employed as the single-degree-of-freedom (SDOF) analytical model, and then the mechanical and geometric parameters of MYDs are derived via the design method from the perspective of the uniform damping ratio. In addition, the gas temperature of the natural fire curves is determined according to current European standards, and 16 representative fire scenarios are selected. Moreover, the residual material properties and residual performance of the primary structure as well as MYD are investigated and expressed in mathematical forms. Thereon, the linear forms of the restoring forces of the primary structure and MYD are obtained by utilizing the equivalent linearization method, and the motion-governing and energy-conservation equations are established. Furthermore, the methodology for the parametric analysis is put forward, and the residual seismic performance of the fire-damaged damped structure is derived quantitatively, which is also verified via time-domain analysis with recorded ground motions. The results show that the seismic performance of the SDOF concrete structure with MYD can be reduced significantly by fire damage. **DOI: 10.1061/(ASCE)ST.1943-541X.0003284.** *© 2022 American Society of Civil Engineers.*

**Author keywords:** Metallic yielding damper (MYD); Concrete structure; Seismic performance; Fire damage; Numerical analysis.

## Introduction

Building structures are vulnerable to various disasters, such as earthquakes, hurricanes, and fire, which could result in severe casualties and property losses (Buchanan and Abu 2017; Kelly et al. 1972). In terms of structural vibration induced by earthquakes or hurricanes, many scholars have devoted themselves to energy-dissipation technologies and put forward working principles and design methods of various dampers (Asai et al. 2017; Gutierrez Soto and Adeli 2013; Ikago et al. 2012; Jia et al. 2019; Kelly et al. 1972; Oliveira et al. 2018; Xu et al. 2018). These dampers can effectively mitigate the structural responses (displacement, acceleration, and interstory drift angle, among others) by either detuning [transferring the energy from structure to tuning device (Gutierrez Soto and Adeli 2013)] and/or damping effects [dissipating (Kelly et al. 1972) or harvesting (Asai et al. 2017) the energy of structure]. Among these dampers, the metallic yielding damper (MYD) firstly introduced by Kelly et al. (1972) has been widely employed owing to its stable performance, simple design methods and construction schemes, and lower material cost (Zhang et al. 2018). Under the excitation of earthquake or hurricane, the MYD is capable of yielding and then entering the plastic stage earlier than structural members, thus dissipating the most of the input seismic energy and protecting building structures.

Regarding structural fire safety, three measures are usually taken into consideration: (1) setting external fireproof barriers around the structural components, (2) printing or spraying fireproof materials for steel members, and (3) increasing the thickness of the concrete cover for RC members. These measures can protect ordinary structural components in a fire effectively. However, when it comes to the structural design to resist multiple hazards, including structural vibration caused by earthquakes and/or hurricanes and the fire disaster, two severe problems might appear, and neither of these problems has been solved satisfactorily so far.

The first problem is that the performance of damped structures could not be guaranteed after being exposed to fire due to three specific reasons:

- Reason 1: Currently, most of the dampers are (partially) made of metals, such as MYDs, tuned liquid/mass dampers, and viscous dampers. These dampers are vulnerable to fire because the

[1]Dept. of Disaster Mitigation for Structures, Tongji Univ., Room B406, Shanghai 200092, China (corresponding author). ORCID: https://orcid.org/0000-0002-3541-5535. Email: jiayingqi@tongji.edu.cn

[2]Dept. of Disaster Mitigation for Structures, Tongji Univ., Room B303, Shanghai 200092, China. Email: wangchao17@tongji.edu.cn

[3]Associate Professor, Dept. of Disaster Mitigation for Structures, Tongji Univ., Room B407, Shanghai 200092, China. Email: lilingzhi@tongji.edu.cn

[4]Associate Professor, Dept. of Disaster Mitigation for Structures, Tongji Univ., Room B312, Shanghai 200092, China. Email: zhangruifu@tongji.edu.cn

[5]Full Professor, Dept. of Disaster Mitigation for Structures, Tongji Univ., Room B408, Shanghai 200092, China. Email: lzd@tongji.edu.cn

Note. This manuscript was submitted on April 24, 2021; approved on October 28, 2021; published online on January 17, 2022. Discussion period open until June 17, 2022; separate discussions must be submitted for individual papers. This paper is part of the ***Journal of Structural Engineering***, © ASCE, ISSN 0733-9445.

elastic modulus and yielding strength of metals can decrease with elevated temperatures (Jia et al. 2020), and thus the damper's performance might also degenerate.

- Reason 2: Primary structures themselves, such as concrete, steel, and timber, as well as composite concrete–steel structures, are also vulnerable to a fire disaster. Taking the widely constructed concrete structure as an example, severe degradations of both concrete and steel materials could occur when exposed to fire (Jia et al. 2020; Maraveas et al. 2017a, b; Ni and Birely 2018; Witek et al. 2006). The elastic modulus and yielding strength of steel bars can be reduced as the temperature increases (Maraveas et al. 2017a, b). Moreover, considering potential fire-induced spalling and cracking of concrete materials (Witek et al. 2006), effective fire protection for steel bars could not be ensured even if a thick concrete cover exists.
- Reason 3: It is not uncommon that a secondary fire disaster occurs following a mainshock (Mazza 2016; Mazza and Vulcano 2010), and the failure of fire prevention might occur in this stage. For instance, the firefighting access could be blocked by building debris, and the supply system of firefighting water might be disconnected by a large relative deformation (Mazza 2017; Mazza and Vulcano 2010; Ni and Birely 2018; Quayyum and Hassan 2018). As a result, the elevation of the temperature might be out of control, which increases the failure probability of both dampers and structures. Consequently, structural safety might be threatened in the cases of fire–earthquake, or mainshock–secondary fire–aftershock.

The second problem is that the material cost or the structural performance is difficult to optimize. In most of the design codes, such as Eurocodes (BSI 2004a, b), American Concrete Institute (ACI) code (ACI 2007), Chinese code (China Ministry of Housing and Urban-Rural Construction 2015), and almost all the references (not listed here), the effects of earthquake and wind, as well as a fire, are taken into consideration separately based on the reliability analysis by using partial factors. In the design process, a structure is devised according to the requirements for structural vibration firstly, and then fireproof barriers are added around the structural members. Or alternatively, a structure is firstly designed to satisfy the requirements for fire safety, and then it will be retrofitted to satisfy the requirements for structural vibration. However, the former scheme can reduce the available space and impair the aesthetic aspects of structures, and the latter will influence the optimal design for structural vibration control.

As shown in Fig. 1, two schemes with the same areas are considered for the design of the cross section of a three-point bending beam. Scheme I (a hollow square box) has a larger second moment of area compared with Scheme II (a solid square box), and therefore a larger bending stiffness can be supplied to resist the vibration. However, the material properties of Scheme I will degrade faster than those of Scheme II in a fire because the temperature of the entire area of Scheme I can reach a high value quickly, whereas the center part of Scheme II remains a lower temperature. From this simple example, one can observe the antagonism between structural vibration control and fire safety. Moreover, an optimal design scheme must exist between Schemes I and II to realize the minimum material cost or the best structural performance.

To provide an important basis to solve the aforementioned two problems in the future (providing a method to evaluate the structural performance for the first problem and optimization indices for the second problem), this study aims at (1) verifying that the seismic performance of the damped structure can be reduced significantly by a fire, and (2) presenting a methodology to predict the residual seismic performance quantitatively. Considering that concrete structures and MYDs have been widely investigated and constructed, one story from a 6-story office building designed according to Chinese code (China Ministry of Housing and Urban-Rural Construction 2015, 2016a) with four MYDs is utilized in this work to implement theoretical and numerical analyses to investigate the residual seismic performance of damped structures exposed to fire.

The organization of this study is as follows. Firstly, the analytical model of the damped structure, including the primary structure and MYD, is given. The gas temperature is determined according to the relevant Eurocode, and 16 fire scenarios are selected. Next, residual material properties and the residual performance of the primary structure and MYD are investigated and expressed in mathematical functions. Moreover, the linear forms of the restoring forces of the primary structure and MYD are obtained by employing the equivalent linearization method, and the motion-governing and energy-conservation equations are established. On top of that, the methodology for the parametric analysis is put forward, and the residual seismic performance of the fire-damaged damped structure is derived quantitatively, which is also verified via time-domain analysis with recorded ground motions. Eventually, a number of conclusions are given.

## Damped Structure and Selected Fire Scenarios

### *Analytical Model of the Damped Structure*

#### Primary Structure and Site Information

Three terminologies should be clarified firstly and distinguished in the whole study: (1) original structure refers to the uncontrolled structure; (2) primary structure refers to the controlled structure itself; and (3) damped structure refers to controlled structure together

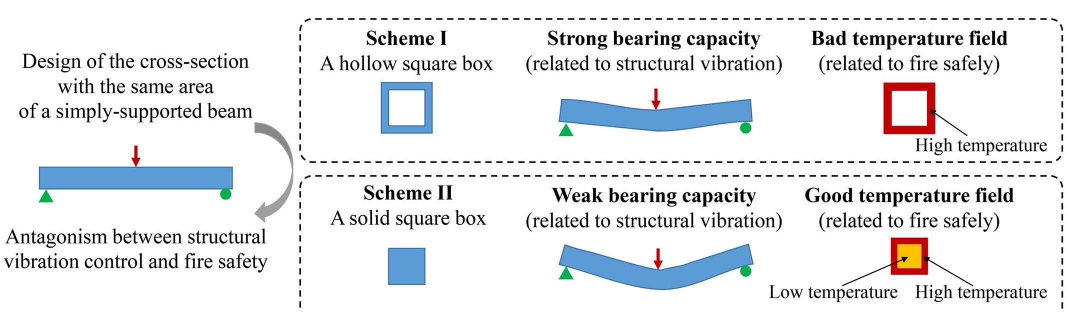


**Fig. 1.** Antagonism between structural vibration control and fire safety in the design of a cross section with the same area of a simply supported beam subject to three-point bending.

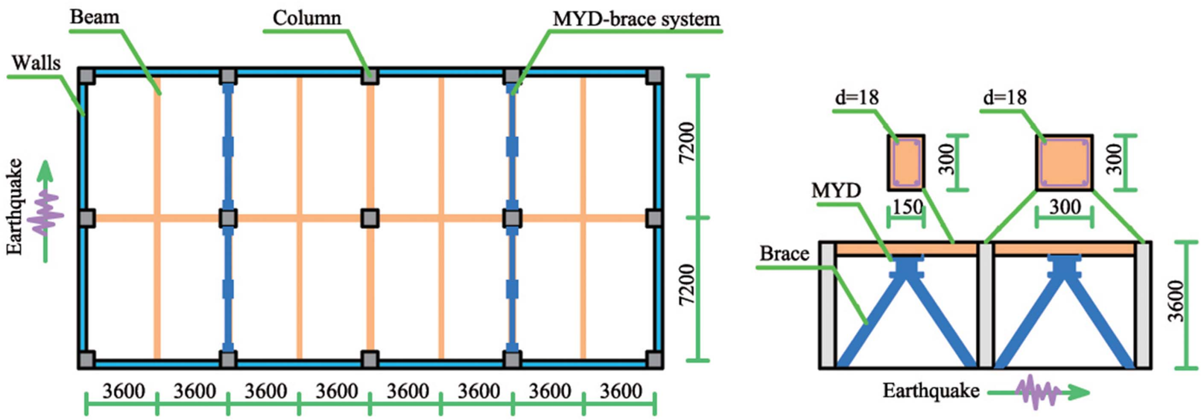


**Fig. 2.** Plan and elevation of the RC structure with MYDs (unit: mm).

with dampers. As shown in Fig. 2, a damped structure is employed to conduct the theoretical and numerical analyses.

In this damped structure, the primary structure is the first story from a 6-story, 5-bay, 2-span RC frame office building in practical engineering without any dampers. This 6-story building was designed based on Chinese codes (China Ministry of Housing and Urban-Rural Construction 2015, 2016a) to meet the design requirements of ultimate and serviceability limit states and was built in Sichuan Province of China in August 1997. Later, it experienced severe damage during the famous Wenchuan earthquake on May 12, 2008. Therefore, it has been used as one of the benchmark models to test the effects of vibration mitigation of external dampers in the structural community.

The current work aims to establish a detailed methodology to analyze the residual performance of fire-damaged damped structures, and thus only the first story is employed herein and adjusted with reasonable and commonly used geometric and material parameters (China Ministry of Housing and Urban-Rural Construction 2015) for rationality and conciseness. The material and part of geometric properties are given in Table 1, and other geometric parameters (in millimeters) are shown in Fig. 2.

The site where the building structure is located is assumed to be classified into Group 2 and Type III based on Chinese code (China Ministry of Housing and Urban-Rural Construction 2016a). In addition, the case of a rare earthquake is studied, and the seismic fortification intensity is assumed as 7.5. That is, first, the equivalent shear-wave velocity $v_{se}$ and the thickness $t_s$ of the overlying soil layer satisfy relationships of $v_{se} \leq 150$ m/s and $15 < t_s \leq 80$ m, or $150 < v_{se} \leq 250$ m/s and $t_s > 50$ m. Second, the design value of the acceleration of ground motion is $0.15g$, and its probability of exceedance is 10% in the 50-year design period. Thirdly, the recurrence interval of the earthquake is 1,600–2,400 years (China Ministry of Housing and Urban-Rural Construction 2016a). On top of that, the predominant period of the site and the peak seismic influence coefficient can be determined as $T_g = 0.55$ s and $\alpha_{\max} = 0.72$ g, respectively.

**Table 1.** Default values of material and geometric properties of the primary structure

| Material or geometric properties | Values |
|---|---|
| Structural mass | 600 t |
| Inherent damping ratio | 0.05 |
| Thickness of the floor slab | 100 mm |
| Yielding strength of steel bars | 400 MPa |
| Elastic modulus of steel bars | 210 GPa |
| Stiffness ratio of steel bars | 0.02 |
| Thickness of the concrete cover of steel bars | 50 mm |
| Peak compressive strength of concrete | 30 MPa |
| Peak compressive strain of concrete | $1.64 \times 10^{-3}$ |
| Ultimate compressive strength of concrete | 15 MPa |
| Ultimate compressive strain of concrete | $3.77 \times 10^{-3}$ |

Source: Data from China Ministry of Housing and Urban-Rural Construction (2015).

### Metallic Yielding Dampers

It can be observed in Fig. 2 that four MYDs will be designed and installed in the existing concrete structure along the direction of the ground motion. In practical engineering, MYDs are usually accompanied by series-connected braces (Fig. 3), and the stiffness of the brace should also be taken into consideration. Thereon, a bilinear hysteresis model is generally utilized as a robust tool to simulate the elastoplasticity of the MYD–brace system (sometimes also referred to as MYD for convenience) (Zhang et al. 2018). In this bilinear hysteresis model (Fig. 3), MYD reaches the yielding state at the displacement $u_{dy}$ with the restoring force $F_{dy}$. Further loading can make the MYD's stiffness reduce from $k_d$ to $\alpha_d k_d$, and the restoring force reaches $F_{d\max}$ when the displacement reaches its maximum $u_{d\max}$.

To give reasonable mechanical parameters of the MYD system for the given primary structure, the design method based on the uniform damping ratio (Zhang et al. 2018) is employed herein owing to its superior conciseness and accuracy. In this method, the equivalent damping ratio $\zeta_{da} = \kappa \cdot \xi$ of the damped structure provided by all the MYDs can be decoupled by the strain energy ratio $\kappa$ (strain energy of all the MYDs to that of the damped structure) and the uniform damping ratio $\xi$. In addition, $\kappa$ and $\xi$ should satisfy

$$\frac{T_{eq,s}^2(1-\kappa)}{4\pi^2}[1-(\zeta_0+\zeta_{s0}(1-\kappa)+\kappa\xi)^2]S_a(T_{eq},\zeta_0+\zeta_{s0}(1-\kappa)+\kappa\cdot\xi)=S_{dt} \quad (1)$$

where $T_{eq,s}$ and $T_{eq}$ = equivalent periods of primary and damped structures, respectively; $\zeta_0$ and $\zeta_{s0}$ = inherent and elastoplastic damping ratios of the primary structure, respectively; and $S_a$ and $S_{dt}$ = spectrum acceleration and target spectrum displacement of the damped structure, respectively.

The detailed procedure to determine the mechanical parameters of MYDs is as follows:

1. Implement the pushover analysis for the primary structure with OpenSEES analytical software version 3.2.2 (McKenna 2011) (Fig. 4), and determine the capacity spectrum in the form of acceleration–displacement response spectrum (Fig. 5).

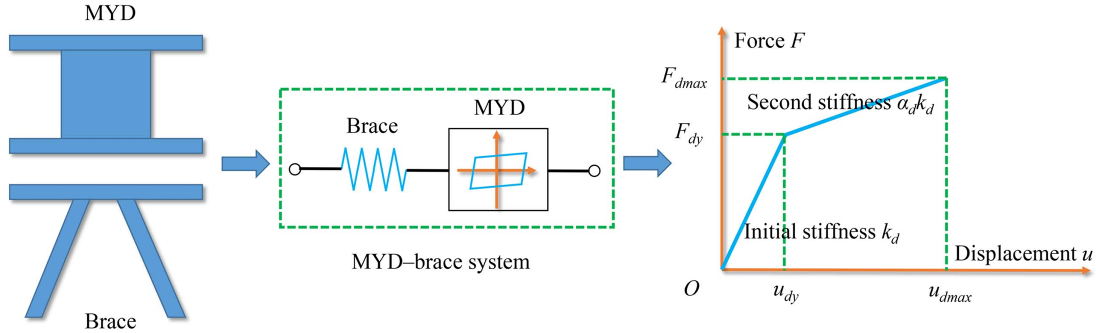


**Fig. 3.** Diagram and force–displacement relationship of the MYD–brace system.

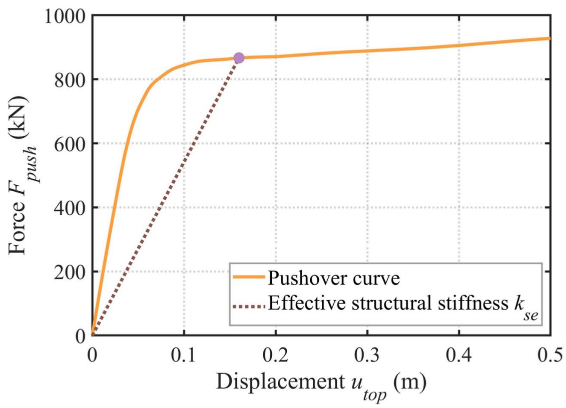


**Fig. 4.** Pushover curve and the effective stiffness $k_{se}$ of the primary structure.

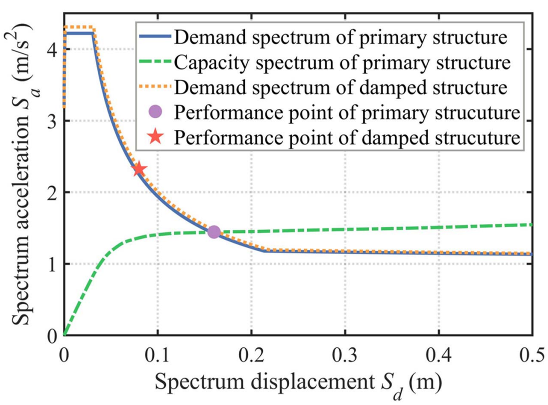


**Fig. 5.** Performance points of primary and damped structures.

2. Determine the demand spectra of primary and damped structures based on the site information (Fig. 5).
3. Determine the spectrum displacement of the primary structure as $S_{d0} = 0.16$ m based on the intersection point of capacity and demand spectra (performance point of primary structure as shown in Fig. 5).
4. Select a reasonable stochastic response mitigation ratio $\sigma_d = S_{dt}/S_{d0} = 0.5$ (Pan and Zhang 2018), and derive the spectrum displacement of the primary structure as $S_{dt} = 0.08$ m (performance point of damped structure as shown in Fig. 5).
5. Given the design ductility factor of MYD $\mu_d = u_{d\max}/u_{dy} = 5$ and the postyielding-to-preyielding stiffness ratio $\alpha_d = 0.005$, parameters $\kappa = 0.460$ and $\xi = 0.200$ can be obtained.
6. Finally, the yielding displacement $u_{dy} = S_{dt}/\mu_d = 0.016$ m and the initial stiffness $k_d = k_{se}\kappa\mu_d/(1-\kappa)/(1+\alpha_d\mu_d-\alpha_d) = 1.07 \times 10^7$ N/m can be obtained, where $k_{se}$ is the effective stiffness of the primary structure (Zhang et al. 2018) (Fig. 4).

Considering the temperature distribution of MYD is related to its three-dimensional topology, it is also necessary to obtain geometric parameters of MYD. Based on the aforementioned mechanical parameters ($k_d$, $u_{dy}$, and $\alpha_d$) of the MYD, the geometric parameters can be derived (Fig. 6) via finite-element analysis with Abaqus software version 6.14 (Dassault Systemes Simulia Corporation 2014) and Python programming (Oliphant 2007) (the latter is employed to enable interaction with Abaqus). In addition, the material properties of MYD are given in Table 2.

## *Selected Fire Scenarios*

To analyze structural fire safety, the fire scenarios must be determined first. The occupation of the current structure is assumed as an office building. Moreover, the whole structure can be regarded as a single fire compartment because the floor area $A_f = 414.72$ m$^2$ is less than the critical value 500 m$^2$ in Eurocode 1 (BSI 2002). Regarding the fire scenarios, ISO 834 curve is widely utilized in standard fire tests, whereas it assumes fuel and gas are exhaustless to keep the fire ongoing (Harmathy and Sultan 1988). To obtain a more accurate fire scenario in the fire compartment within the building structure, the natural fire curve recommended by Eurocode 1 (BSI 2002) is used in this work to determine the gas temperature–time relationships.

### Thermal Absorptivity Coefficient

Before determining the gas temperature, the thermal absorptivity coefficient $b$ of building materials should be calculated first. The thermal absorptivity coefficient $b$ [J/(m$^2 \cdot$ s$^{1/2} \cdot$ °C)] of a single material can be expressed (BSI 2002)

$$b = \sqrt{\rho c \lambda} \in [100, 2{,}200] \tag{2}$$

where $\rho$, $c$, and $\lambda$ = density (kg/m$^3$), specific heat [kJ/(kg · °C)], and thermal conductivity [W/(m · °C)] of the material, respectively. For multiple materials, the thermal absorptivity coefficient can be calculated (BSI 2002)

$$b = \begin{cases} \dfrac{s_1}{s_{\lim}} b_1 + \left(1 - \dfrac{s_1}{s_{\lim}}\right) b_2, & \text{if } b_1 \geq b_2 \text{ and } s_1 \leq s_{\lim} \\ b_1, & \text{else} \end{cases} \tag{3}$$

where $s_i$ = thickness (m) of the $i$th material; $b_i$ = corresponding thermal absorptivity coefficient; subscripts 1 and 2 = materials whose surfaces are exposed to and away from a fire, respectively; and $s_{\lim}$ = critical thickness (m) denoted as follows:

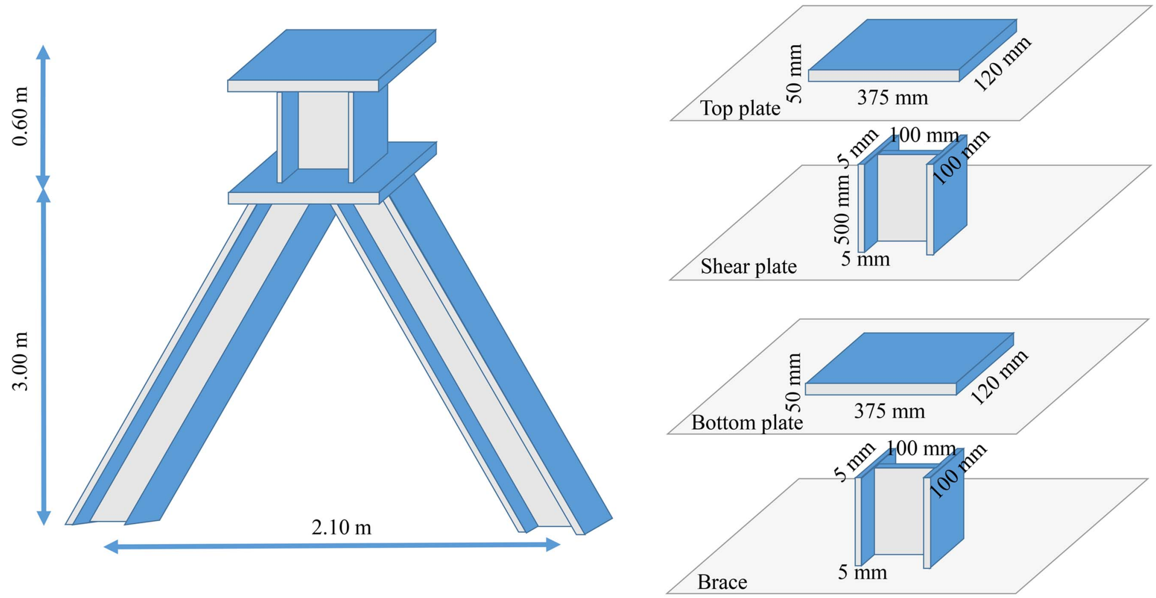


**Fig. 6.** Three-dimensional geometric parameters of MYD.

**Table 2.** Default values of material properties of MYD

| Material properties | Values |
|---|---|
| Yielding strength of MYD | 200 MPa |
| Elastic modulus of MYD | 206 GPa |
| Stiffness ratio of MYD | 0.04 |
| Poisson's ratio of MYD | 0.3 |
| Yielding strength of the brace | 235 MPa |
| Elastic modulus of the brace | 206 GPa |
| Stiffness ratio of the brace | 0.04 |
| Poisson's ratio the brace | 0.3 |

$$s_{\lim} = \sqrt{\frac{3{,}600 t_{\max}\lambda_1}{c_1\rho_1}}$$

$$t_{\max} = \max\{0.2\times 10^{-3} q_{t,d}/O, t_{\lim} = 1/3\}(\mathrm{h}) \tag{4}$$

where $O$ = opening factor related to the total area of vertical openings on all walls; and $q_{t,d}$ = design value of fire load density ($\mathrm{MJ/m^2}$) and expressed

$$q_{t,d} = q_{f,d}A_f/A_t \in [50, 1{,}000] \qquad q_{f,d} = q_{f,k}m_f\delta_{q1}\delta_{q2}\delta_n \tag{5}$$

where $A_t$ and $A_f$ = areas of the entire surfaces and the floor surface of the structure, respectively. The five parameters $q_{f,k} = 511\ \mathrm{MJ/m^2}$, $m_f = 0.8$, $\delta_{q1} = 1.5$, $\delta_{q2} = 1.0$, and $\delta_n = 1.0$ are related to the fire load densities, combustion factor, size of the compartment, type of occupancy (office building in this study), and firefighting measures, respectively.

Considering the structure is composed of varying enclosures (walls, ceiling, and floor) with different thermal absorptivity coefficients, the comprehensive thermal absorptivity coefficient can be written

$$b = \frac{\sum b_j A_j}{A_t - A_v} \tag{6}$$

where $b_j$ and $A_j$ = thermal absorptivity coefficient and area (apart from openings) of the $j$th enclosure, respectively; and $A_v$ = overall area of vertical openings of the building. Regarding the primary structure given in Fig. 2, the thermal coefficient $b = 904.6\ \mathrm{J/(m^2 \cdot s^{1/2} \cdot {}^\circ C)}$ can be obtained, and the calculation process is given in Table 3 (all the units are the same as described previously, respectively).

## Gas Temperature

The gas temperature $T_g$ (°C) in a fire compartment can be computed as follows (BSI 2002):

$$T_g = 20 + 1{,}325 \times (1 - 0.324e^{-0.2t^*} - 0.204e^{-1.7t^*} - 0.472e^{-19t^*}) \tag{7}$$

where $t$ = duration (h) of fire exposure; and $t^* = t\Gamma$ is the time coefficient (h), where $\Gamma = (O/b)^2/(0.04/1{,}160)^2$ is a dimensionless parameter determined by the opening factor $O$ and the aforementioned thermal absorptivity coefficient $b$. The gas temperature will reach its maximum $T_{\max}$ if the fuel or gas is exhausted, and the corresponding time $t^*_{\max}$ is given

$$t^*_{\max} = 0.2\times 10^{-3} q_{t,d}\Gamma/O \tag{8}$$

Regarding the cooling phase when the fuel or gas is exhausted, the gas temperature can be expressed

$$T_g = \begin{cases} T_{\max} - 625(t^* - t^*_{\max}x), & \text{if } t^*_{\max} \le 0.5 \\ T_{\max} - 250(3 - t^*_{\max})(t^* - t^*_{\max}x), & \text{if } 0.5 < t^*_{\max} < 2 \\ T_{\max} - 250(t^* - t^*_{\max}x), & \text{if } t^*_{\max} \ge 2 \end{cases} \tag{9}$$

where $x$ = dimensionless parameter and is expressed

$$x = \begin{cases} 1.0, & \text{if } t_{\max} > t_{\lim} \\ t_{\lim}\Gamma/t^*_{\max}, & \text{if } t_{\max} = t_{\lim} \end{cases} \tag{10}$$

In this study, four reasonable opening factors, namely $O_1 = 0.02$, $O_2 = 0.04$, $O_3 = 0.06$, and $O_4 = 0.08$, are selected to simulate varying possible areas of vertical openings on the walls (Mazza 2015). Then relationships between the gas temperature $T_g$ and the

**Table 3.** Thermal coefficients of the primary structure

| Enclosures | Positions | Materials | $s$ | $\rho$ | $c$ | $\lambda$ | $b_i$ | $b_j$ | $b$ |
|---|---|---|---|---|---|---|---|---|---|
| Walls | Exposed to a fire | Mortar | 0.24 | 1,800 | 1.05 | 0.93 | 1,326 | 341.3 | 904.6 |
| | Away from a fire | Rock wool | 0.05 | 110 | 1.22 | 0.05 | 82 | | |
| Ceiling | Exposed to a fire | Concrete | 0.12 | 2,500 | 0.92 | 1.74 | 2,000 | 243.3 | |
| | Away from a fire | Rock wool | 0.05 | 110 | 1.22 | 0.05 | 82 | | |
| Floor | Exposed to a fire | Marble | 0.02 | 2,800 | 0.92 | 2.91 | 2,738 | 2,009.0 | |
| | Away from a fire | Concrete | 0.12 | 2,500 | 0.92 | 1.74 | 2,000 | | |

Sources: Data from BSI (2002); China Ministry of Housing and Urban-Rural Construction (2016b).



time of fire exposure $t_f$ can be determined according to Eqs. (7) and (9), as shown in Fig. 7.

To demonstrate the aforementioned difference between the natural fire curves and the standard ISO 834 (Harmathy and Sultan 1988) curve, the latter is also shown in Fig. 7. It can be observed that the standard ISO 834 curve can monotonically increase to infinity, whereas the natural fire curves have both the increasing and decreasing phases and thus are more practical than the ISO 834 curve. As shown in Fig. 8, four specific durations of fire exposure, namely, $t_{f1} = 0$, $t_{f2} = t^*_{\max}(O)/3$, $t_{f3} = 2 * t_{\max}/3$, and $t_{f4} = t^*_{\max}(O)$, are selected for each natural fire curve to investigate the residual performance of the damped structure. Therefore, 16 fire scenarios (4 opening factors $O$ × 4 fire exposure duration $t_f$) are taken into consideration in this study.

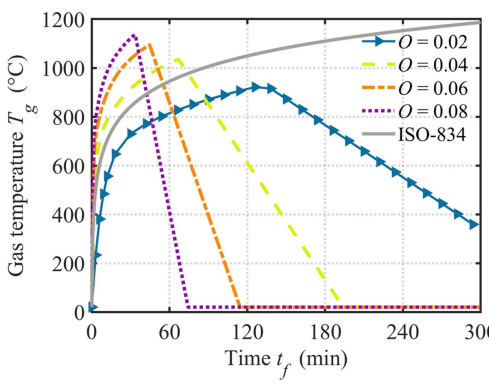


**Fig. 7.** Comparison of the ISO 834 curve and natural fire curves with varying opening factors $O$.

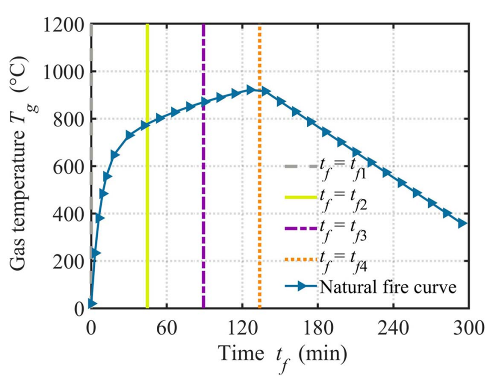


**Fig. 8.** Selection of the duration of fire exposure for a given natural fire curve ($O = 0.02$).

## Residual Seismic Performance of the Primary Structure and MYD

### *Residual Seismic Performance of the Primary Structure*

#### Temperature Field of the Concrete Cross-Section

One direct method to derive the cross-sectional temperature profiles is to implement fire experiments for macroscale structural members (Jin et al. 2018). Moreover, finite-difference or finite-element analyses can be used to conduct heat transfer analysis. These procedures are established according to the energy conservation principle and are not restricted by the materials and shapes of structural members (Li and Deng 2011). However, fire experiments are expensive and time-consuming, and finite-difference and finite-element analyses are complicated to implement. Alternatively, Kodur et al. (2013) have presented a simplified expression based on the regression analysis for the experimental data from fire tests, which can consider different fire exposure conditions and concrete's properties. In the case of multiple surfaces exposed to fire [Fig. 9(a)], the temperature $T$ of a cross-sectional material point with coordinates $(x, y)$ can be expressed (Kodur et al. 2013)

$$T(x,y) = c_2(-1.481\eta_x\eta_y + 0.985(\eta_x + \eta_y) + 0.017)T_g$$

$$\eta_x(x) = 0.155 \ln\frac{t_f}{x^{1.5}} - 0.348\sqrt{x} - 0.371$$

$$\eta_y(y) = 0.155 \ln\frac{t_f}{y^{1.5}} - 0.348\sqrt{y} - 0.371 \tag{11}$$

As for the case of a single surface being exposed to fire [Fig. 9(b)], Eq. (11) can be simplified as follows:

$$T_c(y) = c_1\eta_y T_g \tag{12}$$

In Eqs. (11) and (12), $c_1 = 1.0$ and $c_2 = 1.0$ are material parameters for the normal-strength and carbonate concrete; $\eta_x$ and $\eta_y$ = heat-transfer factors of the fire-exposed surface; $x$ and

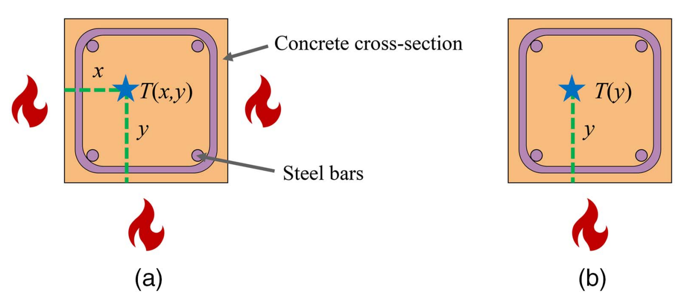


**Fig. 9.** Illustration of the model of Kodur et al. (2013) accounting for the temperature profiles of structural components in the case study: (a) multiple surfaces exposed to a fire; and (b) single surface exposed to a fire.

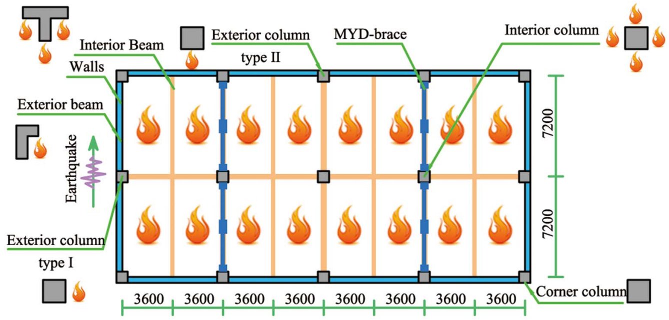


**Fig. 10.** Classification of structural members based on the relative locations in a fire.

$y$ = minimum distances (m) from the material point to fire exposure surfaces; $t_f$ = duration (min) of the fire exposure; and $T_g$ = gas temperature determined by Eqs. (7) and (9).

In this study, the residual properties of the structural members are determined by their temperature fields, and the latter is further controlled by the location of the structural components. As shown in Fig. 10, according to the relative location in a fire, columns can be classified into four types: (1) the interior column with four surfaces exposed to a fire, (2) the exterior Column I with a single surface exposed to a fire, and the normal vector is vertical to its direction of the earthquake, (3) the exterior Column II with a single surface exposed to a fire, and its normal vector is parallel to the direction of the earthquake, and (4) the corner column without any surfaces exposed to a fire. Similarly, beams can also be classified into two types: (1) the interior beam with three surfaces exposed to fire, and (2) the exterior beam with a single surface exposed to a fire.

Moreover, the reinforcement of the floor slab on a beam is also taken into consideration based on the Chinese code (China Ministry of Housing and Urban-Rural Construction 2015). That is, the interior beams are T-shaped and the exterior beams are L-shaped, and the width of a single flange is equal to six times the thickness of the floor slab. According to the classification of structural components, the temperature field can be further determined via Eqs. (11) or (12).

## Residual Properties of the Concrete Cross-Section

**Residual Properties of Concrete**. The stress–strain relationships of the concrete material under varying temperatures are proposed by Eurocode (BSI 2004b), but they might be only useful to calculate the stiffness or capacity of the structural components directly (Kodur et al. 2013). In addition, the 500°C isotherm method can be employed to determine the residual properties of concrete members (BSI 2004b). It is assumed that the fire-damaged depth $d$ is equal to the average thickness of the domain outside the 500°C isotherm profile. Thereon, the cross-section is reduced according to the following rules: the stiffness and strength of inner undamaged concrete can be remained, whereas the outer damaged domain has no contribution to concrete's stiffness and strength. Derived from the 500°C isotherm method for the case of multiple surfaces exposed to a fire, the fire-damaged depth $d$ can be given as follows (Jia et al. 2020):

$$d = \left\{2h' + b' \pm \left[(2h' + b')^2 - 16\int_0^{h'}\int_0^{b'/2}\Gamma(T-500)\mathrm{d}x\mathrm{d}y\right]^{1/2}\right\}\Big/4 \qquad \text{subject to } d \in [0, \min\{b', h'\}] \tag{13}$$

As for the case of a single surface being exposed to a fire, Eq. (13) can be simplified as follows:

$$d = \int_0^l \Gamma(T-500)dx \tag{14}$$

In Eqs. (13) and (14), $b'$ and $h'$ = equivalent cross-sectional width and height under room temperature, respectively; $l = b$ or $l = h$ is the length of the side parallel to the normal vector of the single surface exposed to fire; and $\Gamma()$ = jump function and is defined

$$\Gamma(T-500) = \begin{cases} 1, & T > 500 \\ 0, & T \leq 500 \end{cases} \tag{15}$$

Based on the aforementioned classification of structural members, schematic temperature fields and effective cross-sections of varying numbers of surfaces exposed to a fire are shown in Fig. 11, where $b$ and $h$ are the actual cross-sectional width and height under room temperature (20°C), respectively. According to Fig. 11, the equivalent width $b'$ and height $h'$ can be given as follows:

$$b' = \begin{cases} b, & \text{two surfaces exposed to a fire} \\ \dfrac{b}{2}, & \text{three surfaces exposed to a fire} \\ \dfrac{b}{2}, & \text{four surfaces exposed to a fire} \end{cases},$$
$$h' = \begin{cases} h, & \text{two surfaces exposed to a fire} \\ h, & \text{three surfaces exposed to a fire} \\ \dfrac{h}{2}, & \text{four surfaces exposed to a fire} \end{cases} \tag{16}$$

Substituting Eqs. (16) to (13), or substituting $l = b$ or $l = h$ to Eq. (14), the damaged depth $d$ of the fire-damaged concrete can be derived.

**Residual Properties of Steel Bars**. The properties at elevated temperatures and postfire residual capacities of steel bars are given by many references such as Jia et al. (2020) and Maraveas et al. (2017a, b). For example, the steelwork was classified into three categories by Maraveas et al. (2017b), and the formulas to compute the postfire residual factors of yielding strength, ultimate strength, and elastic modulus are also presented, respectively. Moreover, Maraveas et al. (2017a) presented two alternative formulas accounting for the properties of high-strength steels at elevated temperatures and postfire residual capacities. In addition, the yielding

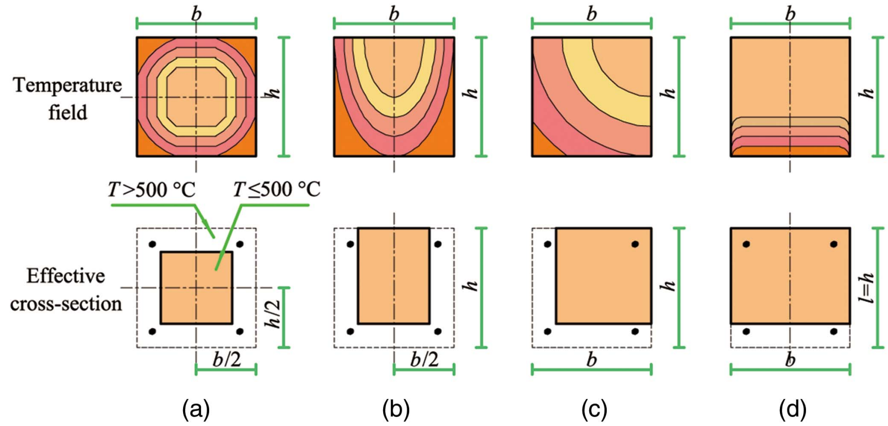


**Fig. 11.** Temperature fields and effective cross-sections of varying numbers of surfaces exposed to a fire: (a) four surfaces; (b) three surfaces; (c) two surfaces; and (d) single surface.

strength and elastic modulus of steel bars under different temperatures are also proposed in Eurocode (BSI 2004b), which are derived from transient- or steady-state fire tests.

Many uncertainties such as the microstructure, manufacturing process, boundary condition, heating duration, and maximum temperature can affect the accurateness of these formulas (Maraveas et al. 2017b). To derive a relatively conservative result in this work, the data of the reduction of the proportional limit (used to represent the yielding strength) and elastic modulus of hot-rolled steel bars at elevated temperatures in the Eurocode (BSI 2004b) are used. Considering the exact formulas of residual properties of steel bars will not affect the conclusions too much, readers can also use the models or experimental data in other literature like Maraveas et al. (2017a, b).

Based on the data in Eurocode (BSI 2004b), the fitting formulas of the yielding strength $f_y(T)$ and the elastic modulus $E_s(T)$ of steel bars under elevated temperatures $T$ are given as follows (Jia et al. 2020):

$$\frac{f_y(T)}{f_{y0}} = 1.057 - 2.510 \times 10^{-3}T + 5.981 \times 10^{-10}T^3 + \frac{5.731 \times 10^{-3}T}{\ln(T)}$$
$$\frac{E_s(T)}{E_{s0}} = (1.027 + 6.105 \times 10^{-11}T^{3.791})^{-1} \tag{17}$$

where $f_{y0}$ and $E_{s0}$ = yielding strength (MPa) and elastic modulus (MPa) of steel bars under room temperature, respectively; and $T$ = temperature at the center of steel bars and can also be determined by Eqs. (11) or (12).

## Residual Seismic Performance

To obtain the primary structure's residual seismic performance, the hysteresis analysis is conducted via OpenSEES software (McKenna 2011). In the hysteresis analysis, concrete-01 and steel-01 constitutive models are used to simulate the concrete material and steel bars, respectively. In addition, the fiber cross-section and the displacement–beam–column element are utilized to simulate the nonlinear behavior of structural members. The detailed information of the OpenSEES model is given in Table 4. Thereon, the hysteresis loops of the fire-damaged primary structure can be shown in Fig. 12. In Fig. 12, the subgraphs correspond to the 16 aforementioned fire scenarios. The fire exposure durations $t_{f1}$–$t_{f4}$ are given from left to right, and opening factors $O_1$–$O_4$ are given from top to bottom.

To conduct the following random vibration analysis in the case study, the nonlinear hysteresis loops of the primary structure should be described in a mathematical form. As a widely investigated hysteresis model, the Bouc-Wen model (Wen 1976) is employed herein to quantify the nonlinear hysteresis properties, which can be expressed

$$F_s = \alpha_s k_s u + (1-\alpha_s)k_s z$$
$$\dot{z} = \frac{1}{\eta}[A\dot{u} - \nu(\gamma|\dot{u}|z|z|^{n-1} - \beta\dot{u}|z|^n)] \tag{18}$$

where $F_s$ = structural restoring force; $k_s$ = initial stiffness coefficient and can be obtained via the pushover analysis; $\alpha_s$ = postyielding to preyielding stiffness ratio; $u$ and $z$ = overall and hysteretic displacements, respectively; $\dot{u}$ and $\dot{z}$ = corresponding time

**Table 4.** Detailed information of OpenSEES model for determining the residual performance of the primary structure

| Parameters | Descriptions | Values | Remarks |
|---|---|---|---|
| ndm | Number of dimensions | 3 | — |
| ndf | Number of degrees of freedom | 6 | — |
| Uniaxialmaterial | Model of steel bars | Steel01 | Data can be obtained from Table 1 and Eq. (17) |
| Uniaxialmaterial | Model of concrete | Concrete01 | Data can be obtained from Table 1 and Eqs. (13) or (14) |
| Section | Model of cross section | Fiber | Mesh size: 0.02 m; concrete cover: 0.05 m |
| Element | Element type | dispBeamColumn | Number of integration points: 8 |
| Constraints | Constraint method | Transformation | — |
| Test | Convergence criterion | EnergyIncr | Tolerance: $1 \times 10^{-20}$; Max iterations: 20 |
| Algorithm | Solution algorithm | Newton | — |
| System | Storage of equation | BandGeneral | — |
| Numberer | Number of degrees of freedom | RCM | — |
| Integrator | Loading method | DisplacementControl | — |
| Analysis | Analytical method | Static | — |



J. Struct. Eng., 2022, 148(4): 04022003

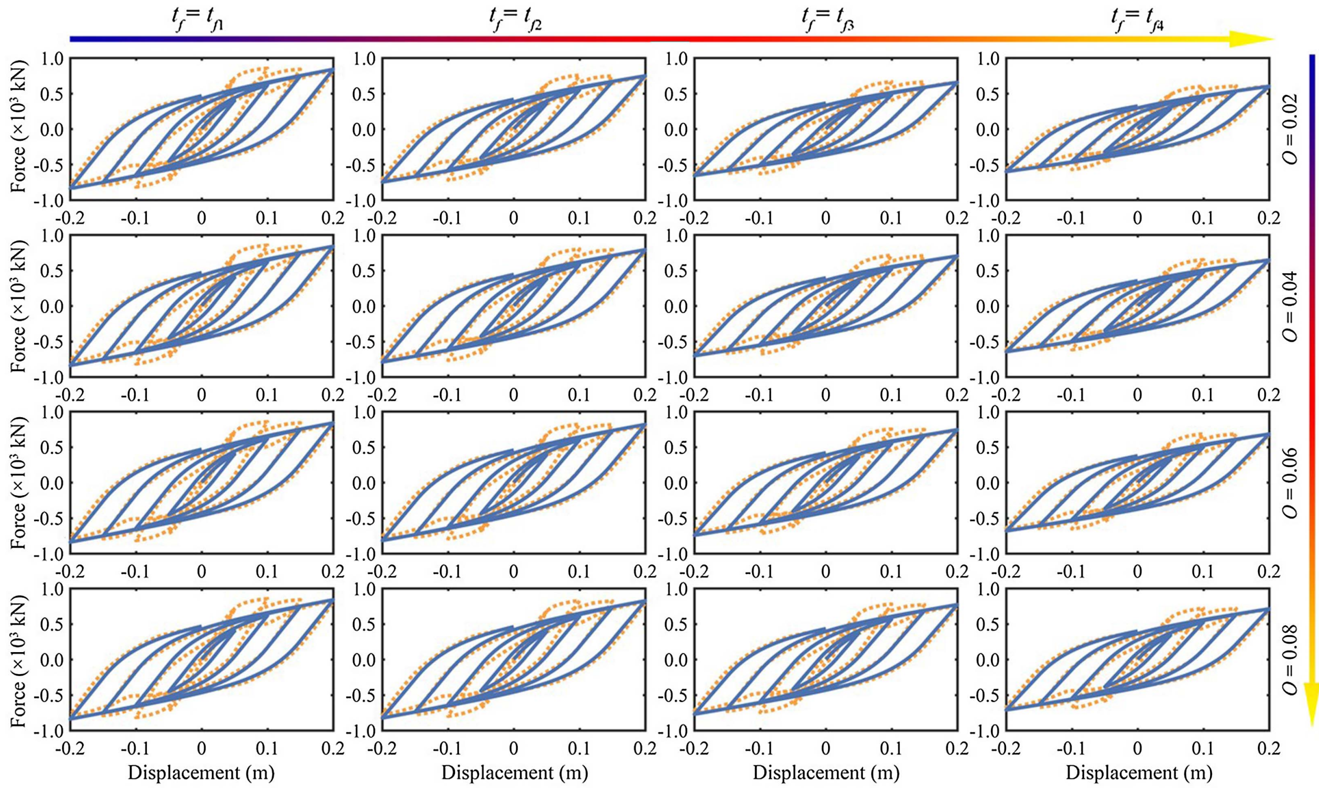


**Fig. 12.** Comparisons between the hysteresis curves of the fire-damaged primary structure obtained from OpenSEES software (dashed lines) and Bouc–Wen model (solid lines).

derivatives; and $\eta$, $A$, $\nu$, $\gamma$, $\beta$, and $n$ = six indices describing the geometric shape of the Bouc-Wen hysteresis curve. As shown in Fig. 13, it can be observed that each of the parameters in Eq. (18) have different control effects to determine the hysteretic loop of the primary structure in the case study. In Fig. 13, the default values are $\eta = 1$, $A = 1$, $\nu = 2$, $\gamma = 5$, $\beta = 0.75$, $n = 1$, $k_s = 300$, and $\alpha_s = 0.2$, and all the other parameters will be unchanged if one of them is varying. Specifically, it can be seen that $\eta$, $A$, and $\nu$ can affect the stiffness and strength of the hysteresis, whereas $\gamma$ and $\beta$ can control the shape of hysteretic loops. Moreover, the smoothness of the transition from elastic to plastic states is influenced by the parameter $n$. As alluded to in the definition, the initial stiffness and stiffness ratio of plastic to elastic phases are determined by parameters $k_s$ and $\alpha_s$, respectively. Therefore, the complicated hysteretic curves obtained from OpenSEES can be represented by the Bouc-Wen model (Wen 1976).

Considering the primary structure is similar to an ideal elastoplastic system, $\eta = \nu = n = 1$ can be assumed (Lin and Zhang 2004). As for other parameters, namely $\alpha_s$, $A$, $\gamma$, and $\beta$, the genetic algorithm [a stochastic optimization algorithm (Chipperfield 1995)] can be utilized as a robust tool to realize the parameter identification by minimizing the errors between the curves from OpenSEES and the Bouc-Wen model in Eq. (18). After the optimization process, the parameters in Eq. (18) can be obtained (not spelled out here), and the Bouc-Wen hysteresis curves are also shown in Fig. 12. It can be observed that the sufficient accuracy of the parameter identification is realized.

## Residual Seismic Performance of MYD

### Temperature Field of MYD

MYDs are usually made of mild steels with lower yield strength, and their thermal properties, density $\rho_s$ (kg/m$^3$), specific heat $C_s$ [J/(kg · °C)] (BSI 2005), thermal conductivity $\lambda_s$ [W/(m · °C)] (Lie and Denham 1993), and thermal expansion coefficient $\alpha_s$ [m/(m · °C)] (BSI 2005) can be given

$$\begin{cases} \rho_s = 7850 \\ C_s = \begin{cases} 2.22\times10^{-6}T^3 - 1.69\times10^{-3}T^2 + 0.773T + 425, & 20 \le T \le 600^\circ\text{C} \\ 13002/(738 - T) + 666, & 600 \le T \le 735^\circ\text{C} \\ 17802/(T) + 545, & 735 \le T \le 900^\circ\text{C} \\ 650, & 900 \le T \le 1200^\circ\text{C} \end{cases} \\ \lambda_s = \begin{cases} -0.022\times T + 48, & 0 \le T \le 900^\circ\text{C} \\ 28.2, & T > 900^\circ\text{C} \end{cases} \\ \alpha_s = 1.4\times10^{-5} \end{cases} \tag{19}$$

To simulate the actual situation, a 2-mm-thick fireproof coating that protects MYD from experiencing excessive fire damage is also taken into consideration. In addition, density, specific heat, and thermal conductivity of the fireproof coating are reasonably selected as

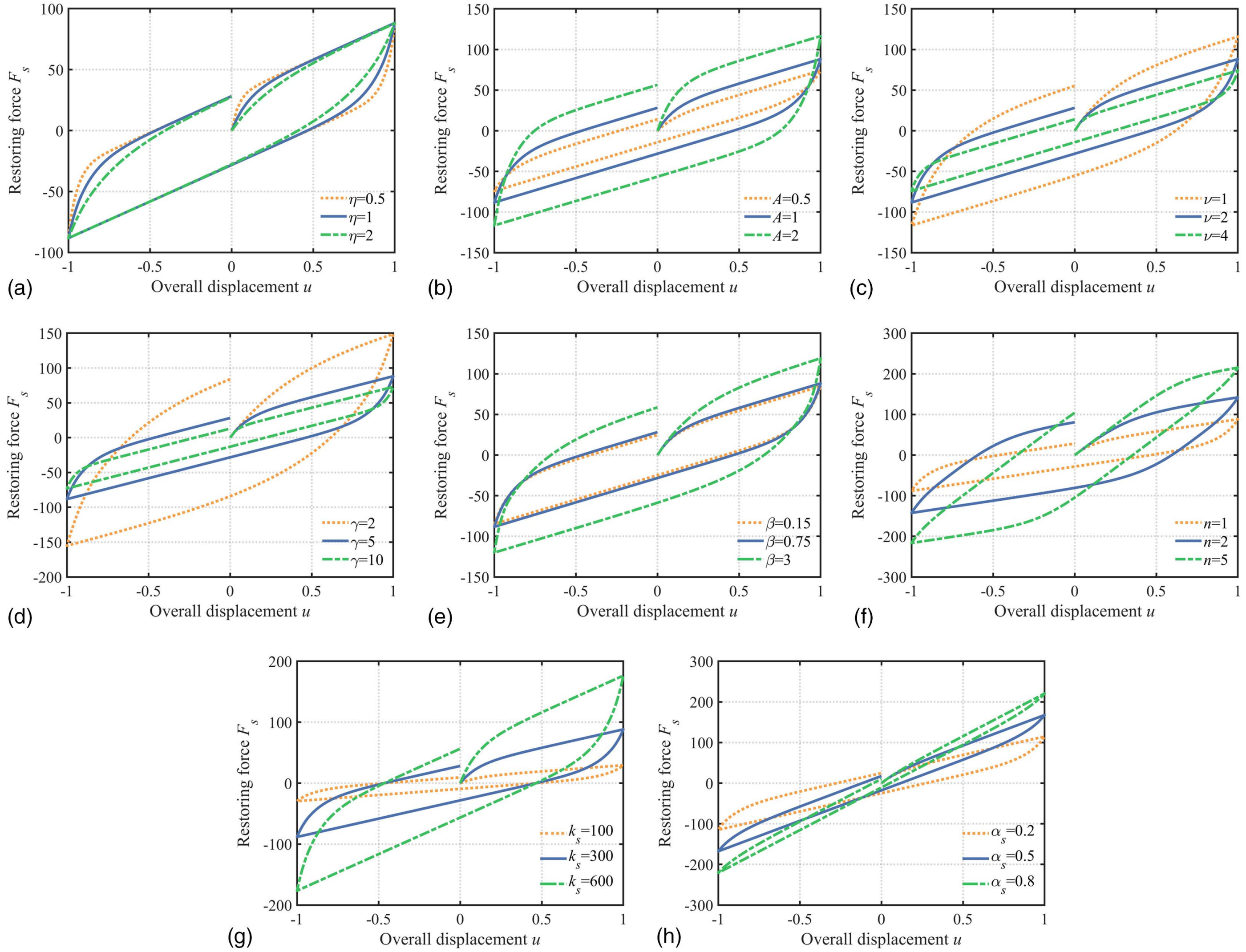


**Fig. 13.** Illustration of control parameters $\eta$, $A$, $\nu$, $\gamma$, $\beta$, $n$, $k_s$, and $\alpha_s$ in the Bouc-Wen model accounting for the residual seismic performance of the primary structure in the case study: (a) varying parameter $\eta$; (b) varying parameter $A$; (c) varying parameter $\nu$; (d) varying parameter $\gamma$; (e) varying parameter $\beta$; (f) varying parameter $n$; (g) varying parameter $k_s$; and (h) varying parameter $\alpha_s$.

$\rho_c = 500\ \mathrm{kg/m^3}$, $C_c = 1{,}000\ \mathrm{J/(kg \cdot ^\circ C)}$, and $\lambda_c = 0.19\ \mathrm{W/(m \cdot ^\circ C)}$, respectively. The residual mechanical properties, i.e., yielding strength and elastic modulus, can be obtained from Table 2 and Eq. (17). Based on these data, the temperature field of MYD under varying fire scenarios can be obtained via thermal analysis with Abaqus software (Dassault Systemes Simulia Corporation 2014), and the detailed information of Abaqus model is given in Table 5.

The model of the MYD–brace system in Abaqus is shown in Fig. 14, and the temperature fields of the MYD–brace system for different fire exposure duration $t_f$ with the opening factor $O = 0.02$ are shown in Fig. 15. The fireproof coating is hidden in Fig. 15, and the scalar variable NT11 represents the temperature field (°C) in the Abaqus software.

## Residual Seismic Performance

To obtain the residual performance of MYD, the hysteresis analysis is conducted via finite-element method with Abaqus software (Dassault Systemes Simulia Corporation 2014) and Python programming (Oliphant 2007). As shown in Fig. 16, two groups of displacement-type loadings (Dirichlet boundary conditions) are employed sequentially to simulate the effects of mainshock and aftershock, respectively. Also, the predefined temperature field [Eq. (7)] is exerted at the intersection of the mainshock and aftershock to simulate the secondary fire disaster. In such a way, the case of mainshock–secondary fire–aftershock can be considered for MYDs. The detailed information of the Abaqus model is given in Table 6.

Thereon, the hysteresis loops of the undamaged (dashed lines) and fire-damaged (solid lines) MYDs can be shown in Fig. 17. In Fig. 17, the subgraphs correspond to the 16 aforementioned fire scenarios. The fire exposure durations $t_{f1}$–$t_{f4}$ are given from left to right, and opening factors $O_1$–$O_4$ are given from top to bottom. It can be seen that the hysteresis loops of fire-damaged MYD become slender with the fire exposure time $t_f$ increasing and the opening factor $O$ decreasing. In addition, the details of the subgraphs in the first row and third column in Fig. 17 are shown in Figs. 18 and 19. In Fig. 18, it can be seen that the hysteresis curve of the undamaged MYD (dashed line) has a spiral form like the isotropic hardening model, whereas the hysteresis curve of the fire-damaged MYD (solid line) behaves like the elastic-perfectly plastic model. In Fig. 19, a significant stress relaxation can be observed at the intersection of the undamaged and fire-damaged hysteresis curves, which results from the predefined temperature field.

**Table 5.** Detailed information of Abaqus model for determining the temperature field of MYD

| Categories | Subclasses | Parameters | Values |
|---|---|---|---|
| Analytical step | | Time period | Determined by Eq. (8) |
| | | Maximum number of increments | 1,000 |
| | | Initial increment | 1.0 |
| | | Minimum increment | $10^{-5}$ |
| | | Maximum increment | 2.0 |
| | | Maximum temperature increment | 10°C |
| Parameter setting for the adiabatic surfaces (facets connected to the floor or ceiling) | Surface film conditions | Film coefficient | $4\ \mathrm{W/(m^2 \cdot {}^\circ C)}$ |
| | | Film coefficient amplitude | Instantaneous |
| | | Sink definition | Uniform |
| | | Sink temperature | 20°C |
| | | Sink amplitude | Instantaneous |
| Parameter setting for the heated surfaces (facets exposed to fire) | Surface film conditions | Film coefficient | $25\ \mathrm{W/(m^2 \cdot {}^\circ C)}$ |
| | | Film coefficient amplitude | Instantaneous |
| | | Sink definition | Uniform |
| | | Sink temperature | 20°C |
| | | Sink amplitude | Determined by Eq. (7) |
| | Surface radiations | Emissivity distribution | Uniform |
| | | Emissivity | 0.8 |
| | | Ambient temperature amplitude | Determined by Eq. (7) |
| Others | | Absolute zero | −273°C |
| | | Stefan–Boltzmann coefficient | $5.67 \times 10^{-8}$ |
| | | Initial temperature | 20°C |
| | | Element type | DC3D8 |



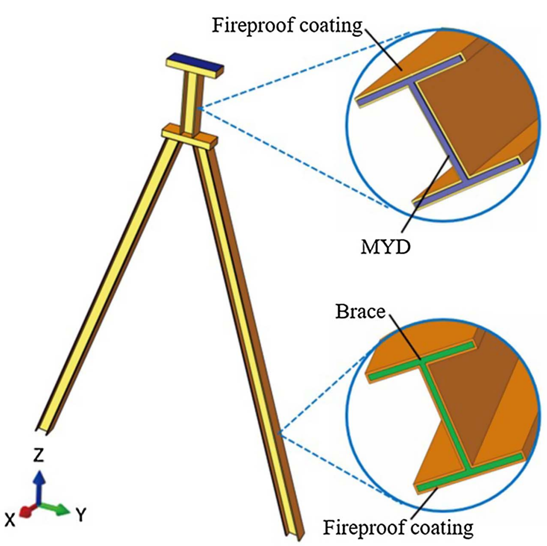


**Fig. 14.** Model of the MYD–brace system with fireproof coatings in Abaqus.

To conduct the random vibration analysis, the bilinear hysteresis model is used to quantitatively describe the nonlinear hysteretic properties of fire-damaged MYDs in the case study, which can be expressed

$$F_d = \alpha_d k_d u + (1-\alpha_d) k_d z$$
$$z = u_{dy} \mathrm{sign}(\dot{u}) \tag{20}$$

where $F_d$ and $k_d$ = restoring force and initial stiffness of MYD, respectively; $\alpha_d$ = stiffness ratio of postyielding to preyielding; $u$ and $z$ = overall and hysteretic displacements of MYD, respectively; and $u_{dy}$ = yielding displacement. Considering the hysteresis curve of the fire-damaged MYD is close to the elastic-perfectly plastic model, the parameters $k_d$, $\alpha_d$, and $u_a$ in Eq. (20) can be easily determined based on Fig. 17 and are not spelled out here.

## Theoretical Analysis

### *Equivalent Linearization of Restoring Forces*

In the previous section, the nonlinearities of the primary structure and MYD can be considered via the Bouc-Wen model in Eq. (18) and the bilinear hysteresis model in Eq. (20), respectively. However, these models are still highly nonlinear and need to be further simplified. Among varying analytical methods, the equivalent linearization method (Hurtado and Barbat 2000) is a powerful tool because of its explicit physical meanings of parameters and concise expressions. Based on certain rules, the nonlinear restoring force can be rewritten in a linear form such that the computational efficiency can be improved.

#### Equivalent Linearization of the Bilinear Hysteresis Model

According to the equivalent linearization method (Hurtado and Barbat 2000), the equivalent hysteretic displacement in Eq. (20) can be denoted

$$\bar{z}_d = c_e \dot{u} + k_e u \tag{21}$$

where $c_e$ and $k_e$ = two unknown coefficients.

Substituting Eq. (21) into Eq. (20) derives the equivalent restoring force

$$F_d = \alpha_d k_d u + (1-\alpha_d) k_d (k_e u + c_e \dot{u}) = \tilde{c}_e \dot{u} + \tilde{k}_e u \tag{22}$$

where $\tilde{c}_e$ and $\tilde{k}_e$ = stochastically equivalent damping and stiffness, respectively, which can be expressed

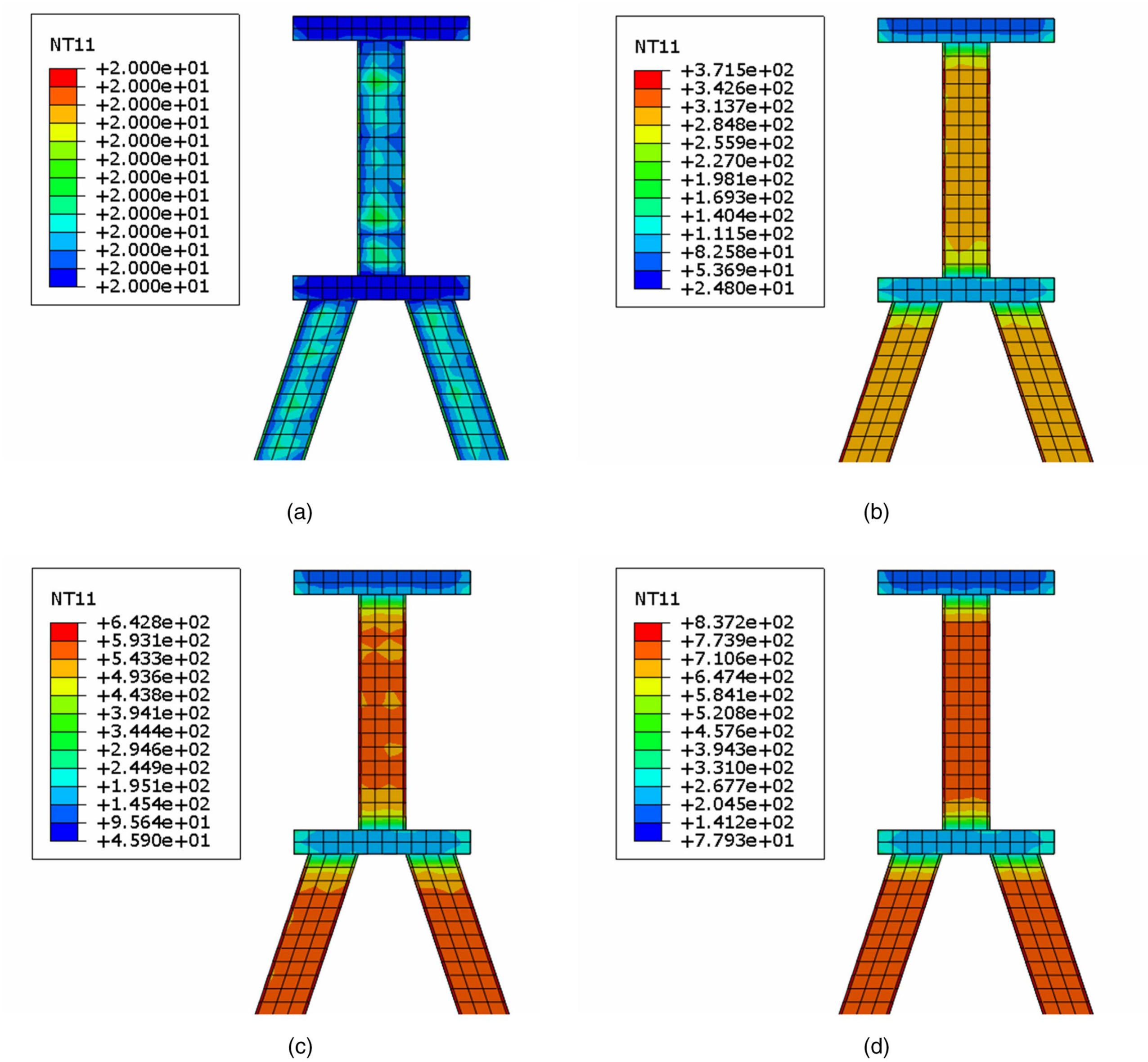


**Fig. 15.** Temperature fields of MYD–brace system for different fire exposure time $t_f$ and $O = 0.02$: (a) $t_{f1} = 0$; (b) $t_{f2} = t^*_{\max}(O)/3$; (c) $t_{f3} = 2 * t_{\max}/3$; and (d) $t_{f4} = t^*_{\max}(O)$.

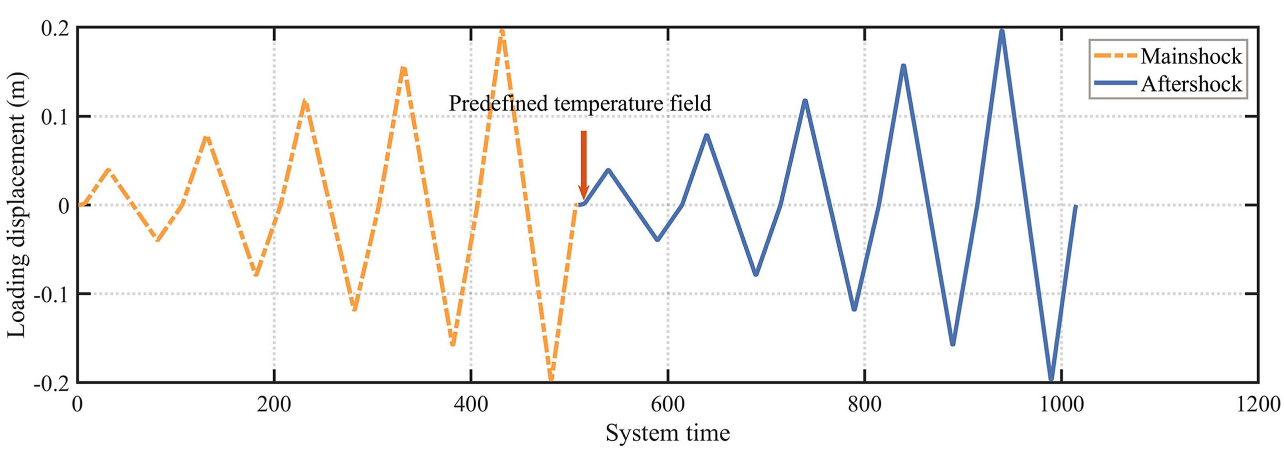


**Fig. 16.** Time histories of the displacement-type loadings and the predefined temperature field.

**Table 6.** Detailed information of Abaqus model for determining the residual performance of MYD

| Categories | Subclasses | Parameters | Values |
|---|---|---|---|
| Analytical steps | Mainshock | Time period | 100 |
| | | Maximum number of increments | 2,000 |
| | | Initial increment | $10^{-2}$ |
| | | Minimum increment | $10^{-5}$ |
| | | Maximum increment | 0.2 |
| | Fire | Time period | 1 |
| | | Maximum number of increments | 100 |
| | | Initial increment | 0.1 |
| | | Minimum increment | $10^{-5}$ |
| | | Maximum increment | 0.2 |
| | Aftershock | Time period | 100 |
| | | Maximum number of increments | 2,000 |
| | | Initial increment | $10^{-2}$ |
| | | Minimum increment | $10^{-5}$ |
| | | Maximum increment | 0.2 |
| Others | | Element type | C3D8R |

$$\tilde{c}_e = (1-\alpha_d)k_d c_e, \tilde{k}_e = \alpha_d k_d + (1-\alpha_d)k_d k_e \tag{23}$$

To achieve a satisfactory linearization, the minimum square error between the nonlinear and linearized terms $E[(\bar{z}_s - z_s)^2] = E[(c_e\dot{x} + k_e x - z_s)^2]$ should be realized, where $E[\cdot]$ represents the expectation operator. Thereon, the unknown coefficients $c_e$ and $k_e$ can be obtained from the expressions

$$\frac{\partial E[(\bar{z}_s - z_s)^2]}{\partial c_e} = 0, \qquad \frac{\partial [E(\bar{z}_s - z_s)^2]}{\partial k_e} = 0 \tag{24}$$

which can be further solved to produce $c_e$ and $k_e$ as follows:

$$c_e = \frac{E[\dot{u}\cdot z_d]}{E[\dot{u}^2]}, \qquad k_e = \frac{E[u\cdot z_d]}{E[u^2]} \tag{25}$$

Substituting Eq. (20) into Eq. (25), parameters $c_e$ and $k_e$ can be obtained

$$c_e = \sqrt{\frac{2}{\pi}}\frac{u_{dy}}{\sigma_{\dot{u}}}, \quad k_e = 0 \tag{26}$$

Substituting Eq. (26) into Eq. (23), stochastically equivalent damping and stiffness coefficients can be written

$$\tilde{c}_e = (1-\alpha_d)k_d\sqrt{\frac{2}{\pi}}\frac{u_{dy}}{\sigma_{\dot{u}}}, \quad \tilde{k}_e = \alpha_d k_d \tag{27}$$

## Equivalent Linearization of the Bouc-Wen Model

Similarly, based on the equivalent linearization method (Hurtado and Barbat 2000), the Bouc-Wen model for the primary structure in Eq. (18) (noting that $\eta = \nu = n = 1$ has already been assumed) can be replaced by

$$F_s = \alpha_s k_s u + (1-\alpha_s)k_s z, \ \dot{z} + p\dot{u} + hz = 0 \tag{28}$$

where $p$ and $h$ = two equivalent linearization parameters and are expressed (Lin and Zhang 2004)

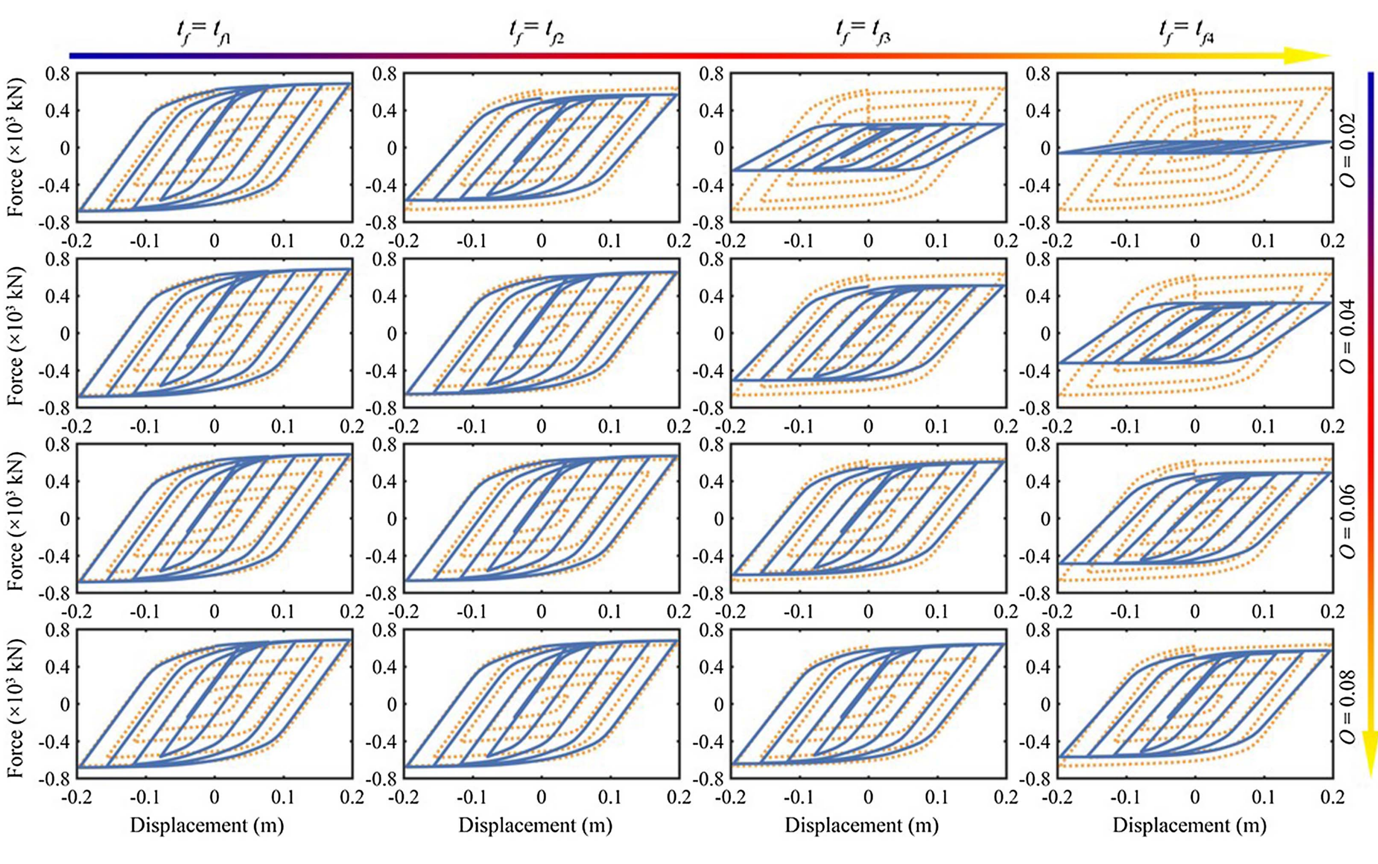


**Fig. 17.** Comparisons between the hysteresis curves of undamaged (dashed lines) and fire-damaged (solid lines) MYDs obtained from Abaqus software and Python programming.



J. Struct. Eng., 2022, 148(4): 04022003

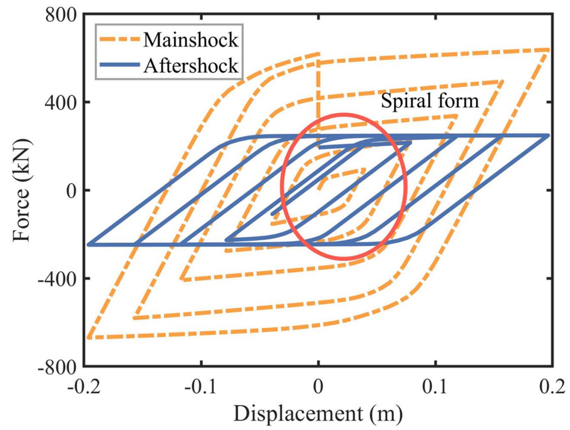


**Fig. 18.** Difference between the hysteresis curves of undamaged (dashed lines) and fire-damaged (solid lines) MYDs.

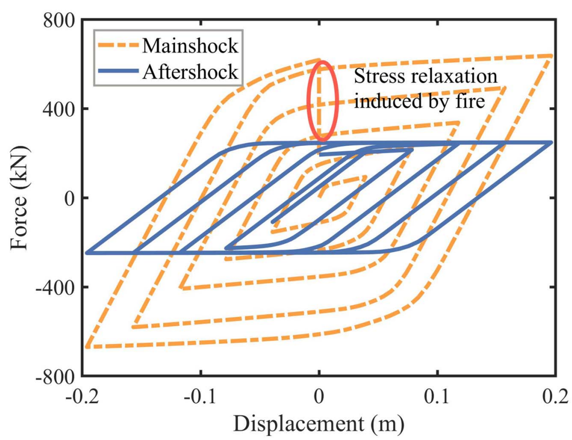


**Fig. 19.** Stress relaxation induced by a fire.

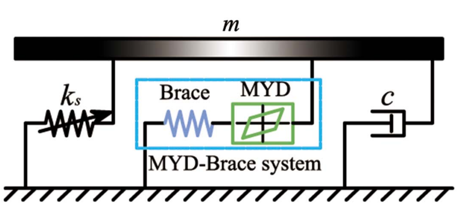


**Fig. 20.** Analytical model of the SDOF damped structure.

$$p = \sqrt{\frac{2}{\pi}}\left(\gamma\frac{\sigma_{\dot{u}z}}{\sigma_{\dot{u}}} + \beta\sigma_z\right) - A, \qquad h = \sqrt{\frac{2}{\pi}}\left(\gamma\sigma_{\dot{u}} + \beta\frac{\sigma_{\dot{u}z}}{\sigma_z}\right) \quad (29)$$

where $\sigma_{\dot{u}}$ and $\sigma_z$ = standard deviations of the velocity $\dot{u}$ and the hysteretic displacement $z$, respectively; and $\sigma_{\dot{u}z}$ = covariance of $\dot{u}$ and $z$.

## *Motion-Governing Equations*

The analytical model of a single-degree-of-freedom (SDOF) damped structure given in Fig. 2 is shown in Fig. 20. The SDOF structure used herein contains a structural mass $m$, a hysteretic structural spring with initial stiffness $k_s$, and structural inherent damping $c$. In addition, the MYD–brace system is also installed in the SDOF structure. Based on the aforementioned equivalent linearization method, the MYD–brace system can be regarded as the combination of an elastic spring $\tilde{k}_e$ and a viscous damping element $\tilde{c}_e$. Thus, the SDOF damped structure shown in Fig. 20 can be substituted with the equivalent one displayed in Fig. 21.

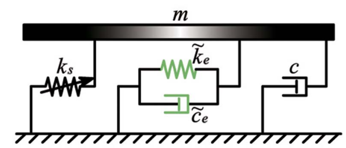


**Fig. 21.** Equivalent model of the SDOF damped structure.

Thereon, the governing equations of the SDOF structure with MYD subjected to a horizontal ground motion can be written

$$\begin{aligned}
& m\ddot{u} + (c + \tilde{c}_e)\dot{u} + (\alpha_s k_s + \tilde{k}_e)u + (1-\alpha_s)k_s z = -m\ddot{u}_g \\
& \dot{z} + p\dot{u} + hz = 0 \\
& p = \sqrt{\frac{2}{\pi}}\left(\gamma\frac{\sigma_{\dot{u}z}}{\sigma_{\dot{u}}} + \beta\sigma_z\right) - A \\
& h = \sqrt{\frac{2}{\pi}}\left(\gamma\sigma_{\dot{u}} + \beta\frac{\sigma_{\dot{u}z}}{\sigma_z}\right) \\
& \tilde{c}_e = (1-\alpha_d)k_d\sqrt{\frac{2}{\pi}}\frac{u_{dy}}{\sigma_{\dot{u}}} \\
& \tilde{k}_e = \alpha_d k_d
\end{aligned} \quad (30)$$

where $\ddot{u}$, $\dot{u}$, and $u$ = structural (also MYD's) acceleration, velocity, and displacement, respectively; and $\ddot{u}_g$ = acceleration of the ground motion, which can be derived based on the Kanai–Tajimi stochastic model and expressed (Rofooei et al. 2001)

$$\ddot{u}_f + 2\xi_f\omega_f\dot{u}_f + \omega_f^2 u_f = -\ddot{w}\,,\ \ddot{u}_g = -2\xi_f\omega_f\dot{u}_f - \omega_f^2 u_f \quad (31)$$

where $\xi_f$ and $\omega_f$ = soil strata's damping coefficient and frequency, respectively; $\ddot{w}$ = white-noise intensity at the rock bed; and $\ddot{u}_f$, $\dot{u}_f$, and $u_f$ = acceleration, velocity, and displacement responses of the soil filter, respectively.

Considering the complexity of the motion-governing equations, the pseudoexcitation method (Lin et al. 1994, 2011; Lin and Zhang 2004) is employed herein to improve the computational efficiency, where stochastic responses can be directly calculated with carefully designed pseudoexcitation. Compared with the classical method of solving the Lyapunov equation, the pseudoexcitation method (Lin and Zhang 2004) is more efficient because the variances or covariances of structural responses are exactly the product of the pseudoresponse and the conjugate, and then the expensive iteration process for solving the overall covariance matrix in Lyapunov method is avoided. According to the pseudoexcitation method, the virtual input seismic excitation can be set as follows:

$$\ddot{\tilde{u}}_g(\omega, t) = \sqrt{S_g(\omega)}e^{i\omega t} \quad (32)$$

where $\omega$ and $t$ = frequency and time of seismic excitation, respectively; $S_g(\omega)$ = power spectral density of excitation; and $i = \sqrt{-1}$ is the imaginary unit. Then, the pseudostructural acceleration $\ddot{\tilde{u}}$, velocity $\dot{\tilde{u}}$, displacement $\tilde{u}$, and hysteretic displacement $\tilde{z}$ can be directly obtained as follows:

$$\tilde{u}(\omega,t)=b(\omega)e^{i\omega t},\qquad \dot{\tilde{u}}(\omega,t)=i\omega b(\omega)e^{i\omega t},\qquad \ddot{\tilde{u}}(\omega,t)=-\omega^2 b(\omega)e^{i\omega t},\qquad \tilde{z}(\omega,t)=b'(\omega)e^{i\omega t} \tag{33}$$

where $b(\omega)$ and $b'(\omega)$ = two amplitudes and are expressed

$$\begin{aligned} b(\omega)&=-\left\{\frac{\alpha_s k_s+\tilde{k}_e}{m}-\omega^2-\frac{(1-\alpha_s)k_s p}{m}\frac{\omega^2}{h^2+\omega^2}+\left[\frac{\omega(c+\tilde{c}_e)}{m}-\frac{(1-\alpha_s)k_s p}{m}\frac{h\omega}{h^2+\omega^2}\right]i\right\}^{-1}\sqrt{S_g(\omega)}\\ b'(\omega)&=-\left(1+\frac{h}{i\omega}\right)^{-1}pb(\omega) \end{aligned} \tag{34}$$

On top of that, the variances of the structural displacement $\sigma_u^2$, velocity $\sigma_{\dot{u}}^2$, acceleration $\sigma_{\ddot{u}}^2$, and hysteretic displacement $\sigma_z^2$, as well as the covariance of velocity and hysteretic displacement $\sigma_{\dot{u}z}$, can be calculated

$$\begin{aligned} \sigma_u^2&=\int_{-\infty}^{+\infty}\tilde{u}(\omega,t)^*\tilde{u}(\omega,t)d\omega=2\int_0^{+\infty}|b|^2 d\omega\\ \sigma_{\dot{u}}^2&=\int_{-\infty}^{+\infty}\dot{\tilde{u}}(\omega,t)^*\dot{\tilde{u}}(\omega,t)d\omega=2\int_0^{+\infty}\omega^2|b|^2 d\omega\\ \sigma_{\ddot{u}}^2&=\int_{-\infty}^{+\infty}\ddot{\tilde{u}}(\omega,t)^*\ddot{\tilde{u}}(\omega,t)d\omega=2\int_0^{+\infty}\omega^4|b|^2 d\omega\\ \sigma_z^2&=\int_{-\infty}^{+\infty}\tilde{z}(\omega,t)^*\tilde{z}(\omega,t)d\omega=2\int_0^{+\infty}|b'|^2 d\omega\\ \sigma_{\dot{u}z}&=\int_{-\infty}^{+\infty}\dot{\tilde{u}}(\omega,t)^*\tilde{z}(\omega,t)d\omega=\int_{-\infty}^{+\infty}(i\omega b)^* b' d\omega \end{aligned} \tag{35}$$

where $(\cdot)^*$ = conjugate complex number of the variable $(\cdot)$.

Finally, the stochastic structural responses $\sigma_u^2$, $\sigma_{\dot{u}}^2$, $\sigma_z^2$, and $\sigma_{\dot{u}z}$ in Eq. (35) can be obtained by iterations until convergence. As for the original (uncontrolled) structure, the amplitude $b(\omega)$ in Eq. (34) can be obtained by setting $\tilde{k}_e=\tilde{c}_e=0$ as follows:

$$b(\omega)=-\left\{\frac{\alpha_s k_s}{m}-\omega^2-\frac{(1-\alpha_s)k_s p}{m}\frac{\omega^2}{h^2+\omega^2}+\left[\frac{\omega c}{m}-\frac{(1-\alpha_s)k_s p}{m}\frac{h\omega}{h^2+\omega^2}\right]i\right\}^{-1}\sqrt{S_g(\omega)} \tag{36}$$

### Energy Conservation Equations

Regarding the principle of energy conservation, the input seismic energy is dissipated by both the primary structure and MYDs. From the perspective of time-domain analysis, the instantaneous energy conservation equation at the time $t$ is given

$$\begin{aligned} e_{\text{total}}(t)&=\sum e_i(t)=\sum e_{\text{structure}}(t)+\sum e_{\text{MYD}}(t)\\ &=e_{k,p}(t)+e_{e,p}(t)+e_{c,p}(t)+e_{d,p}(t)+e_{e,\text{MYD}}(t)\\ &\quad+e_{d,\text{MYD}}(t) \end{aligned} \tag{37}$$

where $e_{\text{total}}(t)$ = input seismic energy at the time $t$; $e_{k,p}(t)$, $e_{e,p}(t)$, $e_{c,p}(t)$, and $e_{d,p}(t)$ = kinetic energy, elastic strain energy, energy dissipated by the inherent damping, and energy dissipated by the elastoplasticity of the primary structure, respectively; and $e_{e,MYD}(t)$ and $e_{d,MYD}(t)$ = elastic strain energy and the energy dissipated by MYD, respectively. Assuming the structural vibration is a stochastic process, then the energy response can be obtained in a stochastic perspective by applying an expectation operator $E[\cdot]$ to both sides of Eq. (37), and we obtain

$$E[e_{\text{total}}(t)]=E[e_{c,p}(t)]+E[e_{d,p}(t)]+E[e_{d,\text{MYD}}(t)] \tag{38}$$

where $E[e_{c,p}(t)]$, $E[e_{d,p}(t)]$, and $E[e_{d,\text{MYD}}(t)]$ can be expressed

$$\begin{aligned} E[e_{c,p}(t)]&=E[c\dot{u}(t)^2]=c\sigma_{\dot{u}}^2\\ E[e_{d,p}(t)]&=E[(1-\alpha_s)k_s z(t)\dot{u}(t)]=(1-\alpha_s)k_s\sigma_{\dot{u}z}\\ E[e_{d,\text{MYD}}(t)]&=E[\tilde{c}_e\dot{u}(t)^2]=E\left[(1-\alpha_d)k_d\sqrt{\frac{2}{\pi}}\frac{u_{dy}}{\sigma_{\dot{u}}}\dot{u}(t)^2\right]\\ &=(1-\alpha_d)k_d\sqrt{\frac{2}{\pi}}u_{dy}\sigma_{\dot{u}} \end{aligned} \tag{39}$$

Finally, the expectation of the total input seismic energy can be written

$$E[e_{\text{total}}(t)]=(1-\alpha_s)k_s\sigma_{\dot{u}z}+c\sigma_{\dot{u}}^2+(1-\alpha_d)k_d\sqrt{\frac{2}{\pi}}u_{dy}\sigma_{\dot{u}} \tag{40}$$

## Parametric Analysis for Residual Seismic Performance

### Indicators for Residual Seismic Performance

To conduct the parametric analysis, the indicators of residual seismic performance should be determined first. In the traditional theories for structural vibration control, the displacement mitigation ratio $\gamma_{u0}$, acceleration mitigation ratio $\gamma_{a0}$, and energy filter ratio $\gamma_{E0}$ under room temperature are defined (Pan and Zhang 2018)

$$\gamma_{u0} = \frac{\sigma_{u0,d}}{\sigma_{u0}}, \quad \gamma_{a0} = \frac{\sigma_{a0,d}}{\sigma_{a0}}, \quad \gamma_{E0} = 1 - \frac{E[e_{d,\mathrm{MYD}}(t)]}{E[e_{\mathrm{total}}(t)]} \tag{41}$$

where $\sigma_{u0,d}$ and $\sigma_{a0,d}$ = root-mean square (RMS) structural displacement and acceleration of the damped structure, respectively; and $\sigma_{u0}$ and $\sigma_{a0}$ = corresponding values of the original structure, respectively. According to the definition, smaller values of $\gamma_{u0}$, $\gamma_{a0}$, and $\gamma_{E0}$ represent better performance to control the structural responses.

To account for the damage induced by a fire, the aforementioned indicators can be rewritten

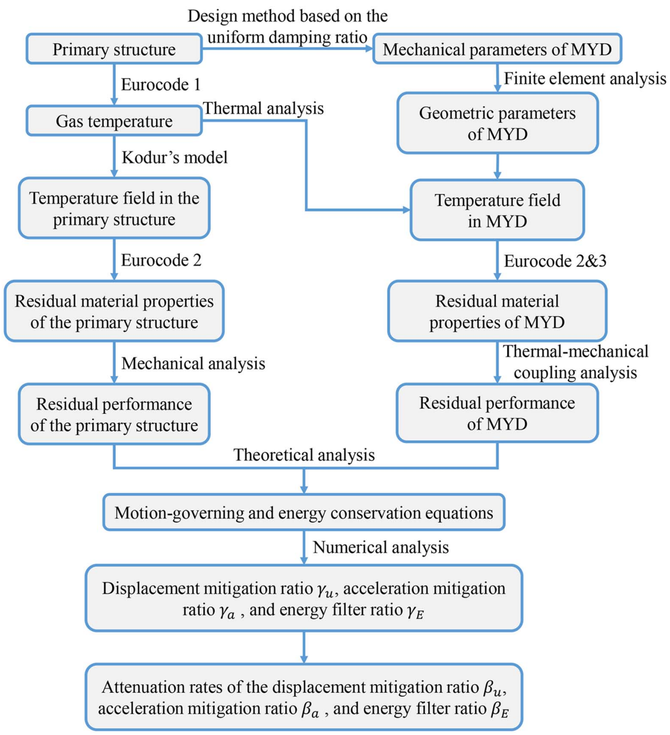


**Fig. 22.** Methodology to investigate the residual seismic performance of the fire-damaged damped structure.

$$\gamma_u(t_f, O) = \frac{\sigma_{u,d}(t_f, O)}{\sigma_{u0}},$$
$$\gamma_a(t_f, O) = \frac{\sigma_{a,d}(t_f, O)}{\sigma_{a0}},$$
$$\gamma_E(t_f, O) = 1 - \frac{E[e_{d,\mathrm{MYD}}(t, t_f, O)]}{E[e_{\mathrm{total}}(t, t_f, O)]} \tag{42}$$

where $O$ = opening factor; and $t$ and $t_f$ = time of seismic excitation and fire exposure, respectively. It can be shown that $\gamma_u(t_f, O) = \gamma_{u0}$, $\gamma_a(t_f, O) = \gamma_{a0}$, and $\gamma_E(t_f, O) = \gamma_{E0}$ for $t_f = 0$.

In this study, three attenuation rates are also defined to investigate the residual performance of the fire-damaged damped structure and are expressed

$$\beta_u(t_f, O) = \frac{\gamma_{u0} - \gamma_u(t_f, O)}{\gamma_{u0}},$$
$$\beta_a(t_f, O) = \frac{\gamma_{a0} - \gamma_a(t_f, O)}{\gamma_{a0}},$$
$$\beta_E(t_f, O) = \frac{\gamma_{E0} - \gamma_E(t_f, O)}{\gamma_{E0}} \tag{43}$$

**Table 7.** Specific values of performance indicators $\gamma_u$, $\gamma_a$, and $\gamma_E$ of the fire-damaged damped structure

| Indicators | Opening factors, $O$ | $t_{f1}$ | $t_{f2}$ | $t_{f3}$ | $t_{f4}$ |
|---|---|---|---|---|---|
| $\gamma_u(t_f, O)$ | 0.02 | 0.711 | 0.760 | 0.897 | 0.975 |
| | 0.04 | 0.711 | 0.725 | 0.785 | 0.865 |
| | 0.06 | 0.711 | 0.722 | 0.748 | 0.794 |
| | 0.08 | 0.711 | 0.720 | 0.731 | 0.760 |
| $\gamma_a(t_f, O)$ | 0.02 | 0.736 | 0.784 | 0.908 | 0.978 |
| | 0.04 | 0.736 | 0.751 | 0.808 | 0.881 |
| | 0.06 | 0.736 | 0.738 | 0.774 | 0.818 |
| | 0.08 | 0.736 | 0.733 | 0.757 | 0.786 |
| $\gamma_E(t_f, O)$ | 0.02 | 0.325 | 0.395 | 0.683 | 0.913 |
| | 0.04 | 0.325 | 0.343 | 0.435 | 0.601 |
| | 0.06 | 0.325 | 0.330 | 0.375 | 0.450 |
| | 0.08 | 0.325 | 0.324 | 0.349 | 0.392 |

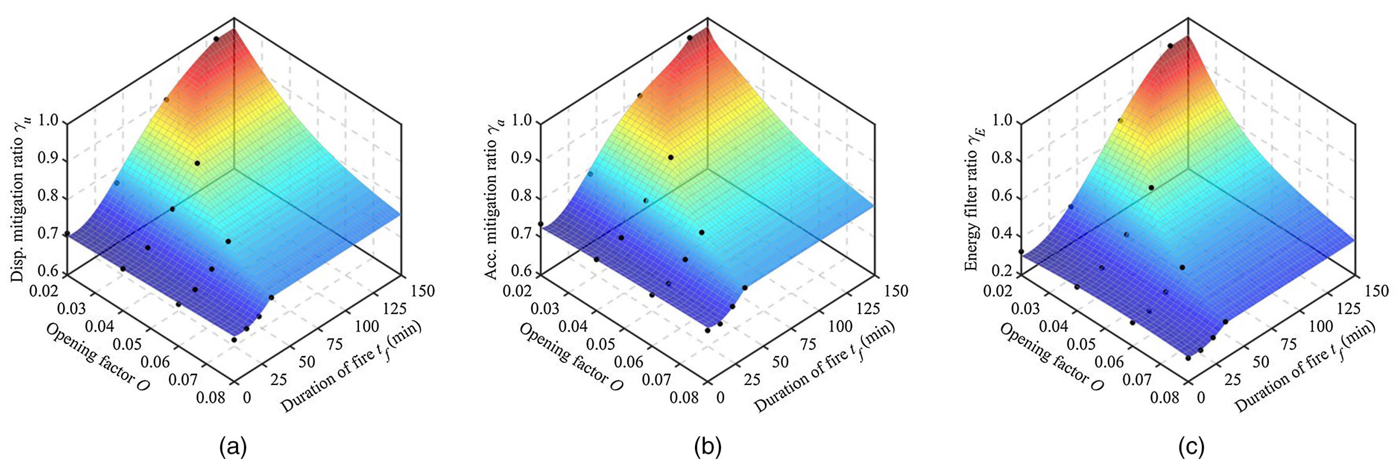


**Fig. 23.** Performance indicators $\gamma_u$, $\gamma_a$, and $\gamma_E$ of the fire-damaged damped structure: (a) displacement mitigation ratio $\gamma_u$; (b) acceleration mitigation ratio $\gamma_a$; and (c) energy filter ratio $\gamma_E$.

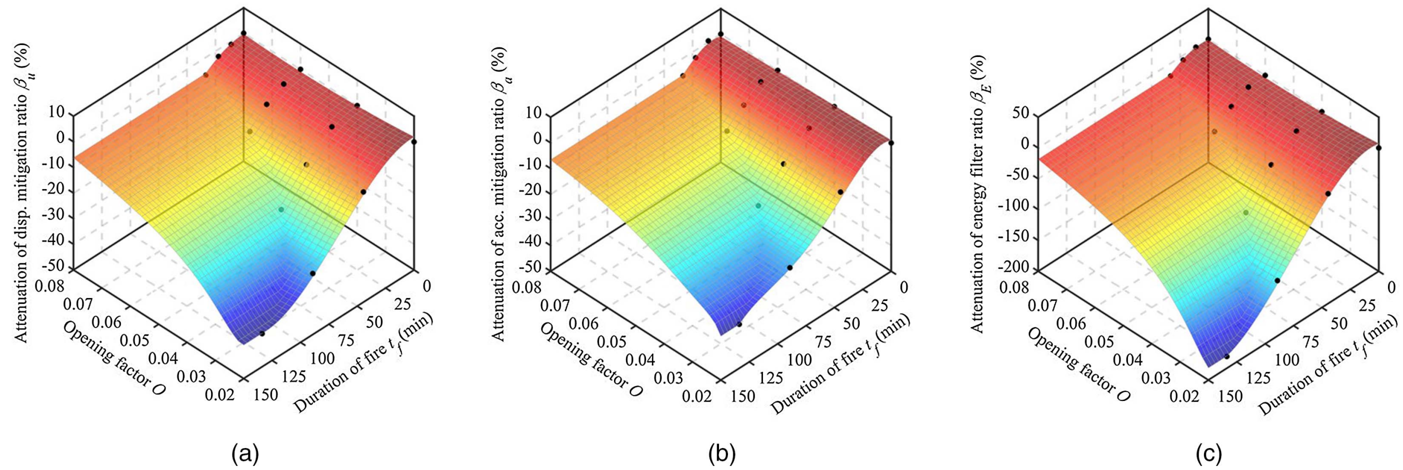


**Fig. 24.** Performance indicators $\beta_u$, $\beta_a$, and $\beta_E$ of the fire-damaged damped structure: (a) attenuation rate of the displacement mitigation ratio $\beta_u$; (b) attenuation rate of the acceleration mitigation ratio $\beta_a$; and (c) attenuation rate of the energy filter ratio $\beta_E$.

**Table 8.** Specific values of performance indicators $\beta_u$, $\beta_a$, and $\beta_E$ of the fire-damaged damped structure

| Indicators | Opening factors, $O$ | $t_{f1}$ (%) | $t_{f2}$ (%) | $t_{f3}$ (%) | $t_{f4}$ (%) |
|---|---|---|---|---|---|
| $\beta_u(t_f, O)$ | 0.02 | 0.0 | −6.9 | −26.2 | −37.0 |
| | 0.04 | 0.0 | −2.0 | −10.4 | −21.6 |
| | 0.06 | 0.0 | −1.5 | −5.2 | −11.6 |
| | 0.08 | 0.0 | −1.2 | −2.8 | −6.9 |
| $\beta_a(t_f, O)$ | 0.02 | 0.0 | −6.6 | −23.4 | −32.9 |
| | 0.04 | 0.0 | −2.1 | −9.8 | −19.7 |
| | 0.06 | 0.0 | −0.3 | −5.2 | −11.1 |
| | 0.08 | 0.0 | 0.4 | −2.9 | −6.8 |
| $\beta_E(t_f, O)$ | 0.02 | 0.0 | −21.5 | −110.1 | −180.7 |
| | 0.04 | 0.0 | −5.4 | −33.7 | −84.8 |
| | 0.06 | 0.0 | −1.5 | −15.4 | −38.4 |
| | 0.08 | 0.0 | 0.2 | −7.5 | −20.4 |

According to the definitions of attenuation rates in Eq. (43), it holds $\beta_u = \beta_a = \beta_E = 0$ for $t_f = 0$, indicating the damped structure is undamaged. Otherwise, attenuation rates $\beta_u$, $\beta_a$, and $\beta_E$ are positive values representing the performance degradation. Based on the aforedefined indicators, the parametric analysis can be summarized as follows:

$$t_f \in \{t_{f,i}\},$$
$$O \in \{O_j\} \rightarrow \{\gamma_u, \gamma_a, \gamma_E, \beta_u, \beta_a, \beta_E\}, \quad \text{for } i, j = 1, 2, 3, 4 \qquad (44)$$

### Methodology for the Parametric Analysis

Based on the model of the damped structure and 16 fire scenarios, the primary structure's and MYD's residual seismic performance, as well as the motion-governing and energy-conservation equations, the methodology for the parametric analysis to investigate the residual seismic performance of the fire-damaged damped structure can be summarized as shown in Fig. 22.

### Numerical Results of the Performance Indicators

Based on the methodology given in Fig. 22, the residual performance of the fire-damaged damped structure can be obtained quantitatively. As shown in Figs. 23(a–c), a series of surface plots are given with the opening factor $O$ on the $x$-axis, duration of fire exposure $t_f$ on the $y$-axis, and performance indicators ($\gamma_u$, $\gamma_a$, and $\gamma_E$) on the $z$-axis. In Fig. 23, the solid points correspond to the 16 predefined fire scenarios, and the surfaces are obtained by fitting the solid points. The performance indicators $\gamma_u$, $\gamma_a$, and $\gamma_E$ are assumed to remain unchanged for $t_f \geq t_{f4} = t^*_{\max}$.

In addition, the specific values of performance indicators are given in Table 7. It can be seen from Fig. 23 or Table 7 that performance indicators $\gamma_u$, $\gamma_a$, and $\gamma_E$ increase with the opening factor $O$ decreasing and the duration of fire exposure $t_f$ increasing, indicating the structural control effects of the damped structure are affected by the fire scenarios.

To display the performance reduction, performance indicators $\beta_u$, $\beta_a$, and $\beta_E$ are shown in Figs. 24(a–c), where the opening factor $O$ is on the $x$-axis, the duration of fire exposure $t_f$ is on the $y$-axis, and performance indicators ($\beta_u$, $\beta_a$, and $\beta_E$) are on the $z$-axis. Similar to Fig. 23, the solid points correspond to the predefined fire scenarios, and the surfaces are obtained by fitting the solid points.

In addition, the specific values of performance indicators are also given in Table 8. It can be observed that the residual performance of the fire-damaged damped structure decreases with the time $t_f$ increasing and the opening factor $O$ decreasing. In the worst scenario ($O = 0.02$ and $t_f = t_{f4}$), the seismic performance of the damped structure can be reduced by 180.7%.

### Power Spectral Density Functions

To account for the variations of the spectral characteristics due to a fire, the power spectral density functions (PSDFs) of the structural displacement $S_u$ and acceleration $S_a$ under varying fire scenarios are shown in Figs. 25 and 26, respectively. In these figures, the PSDF curves of the undamaged original structure are also plotted. In each subgraph (the opening factor $O$ is fixed), it can be seen that the peak of the curve moves up to the left with the fire exposure time $t_f$ increasing, indicating the greater structural response and the worse structural control effect. Specifically, it can be observed that the PSDF curves for $t_f = t_{f4}$ and $O = 0.02$ in Figs. 25(a) and 26(a) are higher than the PSDF curves of the undamaged original structure at certain excitation frequencies, indicating that a severe damping failure occurs because the residual performance of the damped structure is even worse than the uncontrolled structure.

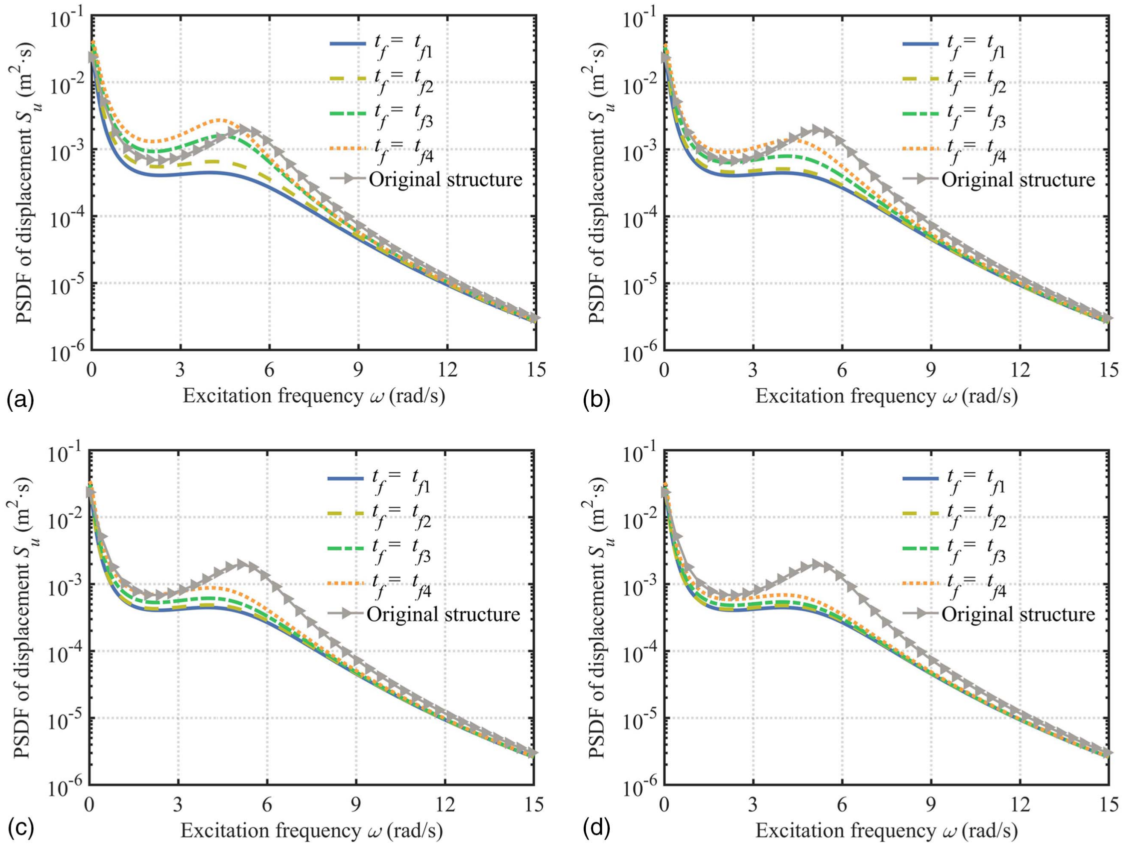


**Fig. 25.** PSDFs of the structural displacement $S_u$ under varying fire scenarios: (a) $O = 0.02$; (b) $O = 0.04$; (c) $O = 0.06$; and (d) $O = 0.08$.

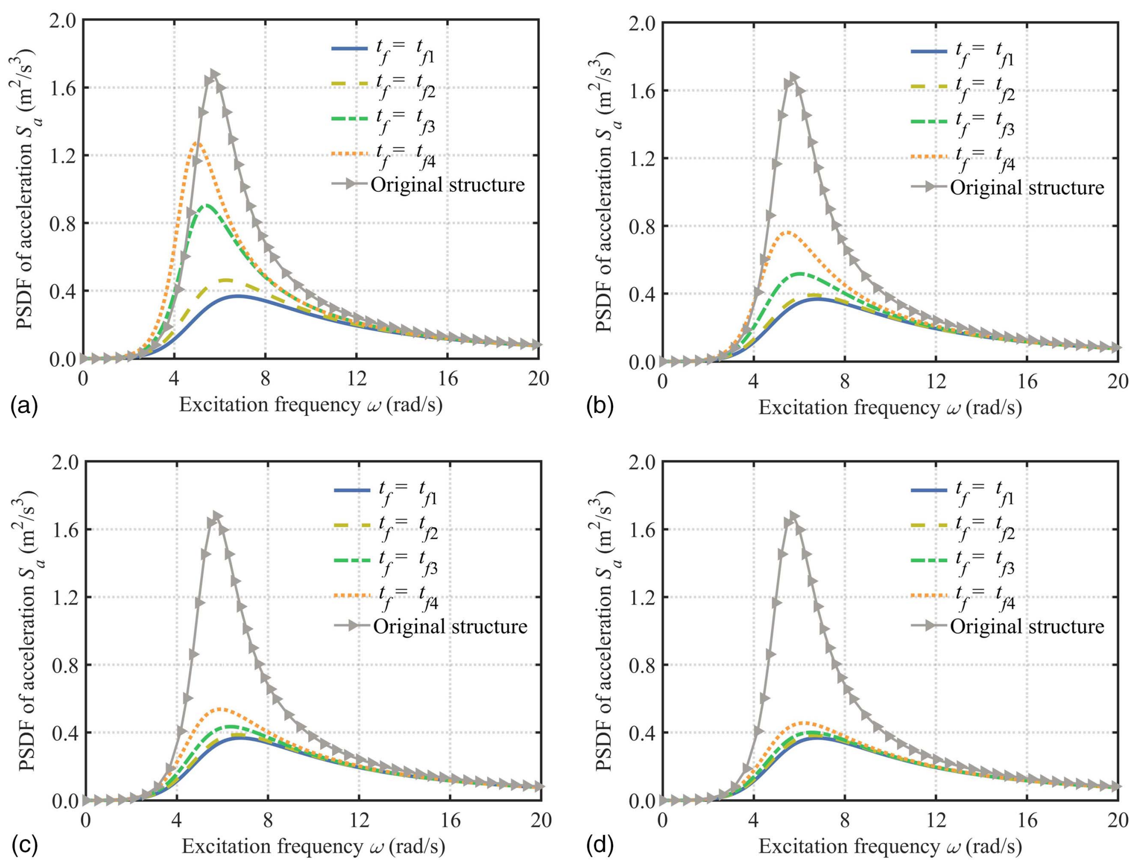


**Fig. 26.** PSDFs of the structural acceleration $S_a$ under varying fire scenarios: (a) $O = 0.02$; (b) $O = 0.04$; (c) $O = 0.06$; and (d) $O = 0.08$.

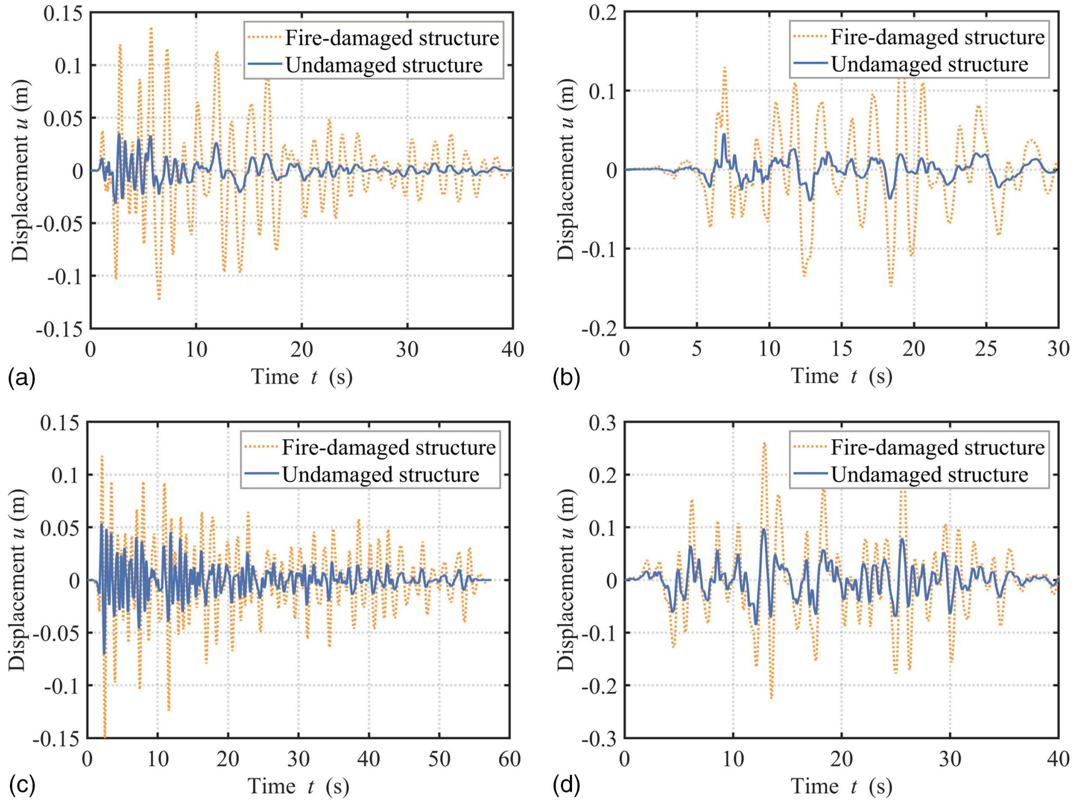


**Fig. 27.** Time histories of the structural displacement under varying ground motions: (a) Ground motion 1; (b) Ground motion 2; (c) Ground motion 3; and (d) Ground motion 4.

**Table 9.** RMS mitigation ratios $\gamma_u$ and attenuation rates $\beta_u$ of structural displacement responses

| Indicator | GM No. | $t_{f1}$ | $t_{f2}$ | $t_{f3}$ | $t_{f4}$ |
|---|---|---|---|---|---|
| $\gamma_u = \dfrac{\sigma_u(t_f, O)}{\sigma_{u0}}$ | GM 1 | 0.220 | 0.317 | 0.663 | 1.024 |
| | GM 2 | 0.257 | 0.351 | 0.748 | 1.113 |
| | GM 3 | 0.341 | 0.415 | 0.658 | 0.863 |
| | GM 4 | 0.420 | 0.522 | 0.845 | 1.072 |
| $\beta_u = \dfrac{\gamma_{u0} - \gamma_u}{\gamma_{u0}}$ (%) | GM 1 | 0.0 | −44.5 | −202.0 | −366.3 |
| | GM 2 | 0.0 | −36.5 | −191.2 | −333.3 |
| | GM 3 | 0.0 | −21.8 | −93.1 | −153.2 |
| | GM 4 | 0.0 | −24.3 | −101.0 | −155.2 |
| Average of $\beta_u$ (%) | — | 0.0 | −31.8 | −146.8 | −252.0 |

Note: GM = ground motion.

**Table 10.** Peak mitigation ratios $\gamma_{Pu}$ and attenuation rates $\beta_{Pu}$ of structural displacement responses

| Indicator | GM No. | $t_{f1}$ | $t_{f2}$ | $t_{f3}$ | $t_{f4}$ |
|---|---|---|---|---|---|
| $\gamma_{Pu} = \dfrac{P_u(t_f, O)}{P_{u0}}$ | GM 1 | 0.248 | 0.367 | 0.698 | 0.962 |
| | GM 2 | 0.295 | 0.395 | 0.728 | 1.082 |
| | GM 3 | 0.392 | 0.474 | 0.719 | 0.837 |
| | GM 4 | 0.439 | 0.555 | 0.918 | 1.176 |
| $\beta_{Pu} = \dfrac{\gamma_{Pu0} - \gamma_{Pu}}{\gamma_{Pu0}}$ (%) | GM 1 | 0.0 | −48.0 | −181.6 | −288.0 |
| | GM. 2 | 0.0 | −33.8 | −146.8 | −266.7 |
| | GM 3 | 0.0 | −20.9 | −83.3 | −113.3 |
| | GM 4 | 0.0 | −26.3 | −109.0 | −167.7 |
| Average of $\beta_{Pu}$ (%) | — | 0.0 | −32.2 | −130.2 | −208.9 |

Note: GM = ground motion; $P_u$ and $P_{u0}$ = peak displacements of fire-damaged and undamaged damped structures, respectively; and $\gamma_{Pu0}$ = mitigation ratio of the peak displacement of the undamaged damped structure.

## Verification with Recorded Ground Motions

### *Time Histories of Structural Displacements*

To further verify the results obtained from the parametric analysis, three recorded and one artificial waves of ground motion are used to conduct the time-domain analysis. These four ground motions were also used in previous work (Jia et al. 2019) representing the diversity of geographical conditions. Based on the Newmark-$\beta$ algorithm, the displacement time histories of the damped structure under varying ground motions can be shown in Fig. 27. In each subgraph, the fire-damaged damped structure for $O = 0.02$ and $t_f = t_{f4}$, as well as the undamaged damped structure for $O = 0.02$ and $t_f = t_{f1}$ are plotted.

Based on these time histories of displacements, RMS and peak mitigation ratios ($\gamma_u$ and $\gamma_{Pu}$) and attenuation rates ($\beta_u$ and $\beta_{Pu}$) can be obtained as given in Tables 9 and 10, respectively. It can be observed that the structural vibration control effects on both RMS and peak displacements can degrade significantly due to the fire damage. For the case of $t_f = t_{f4}$, the residual performance in terms of the control effects on RMS and peak displacements are reduced by 252.0% and 208.9%, respectively.

### *Time Histories of Structural Accelerations*

The acceleration time histories of the damped structures under varying ground motions are shown in Fig. 28. In each subgraph, the fire-damaged damped structure for $O = 0.02$ and $t_f = t_{f4}$, as well as the undamaged damped structure for $O = 0.02$ and $t_f = t_{f1}$ are plotted.

Based on these time histories of accelerations, RMS and peak mitigation ratios ($\gamma_a$ and $\gamma_{Pa}$) and attenuation rates ($\beta_a$ and $\beta_{Pa}$)

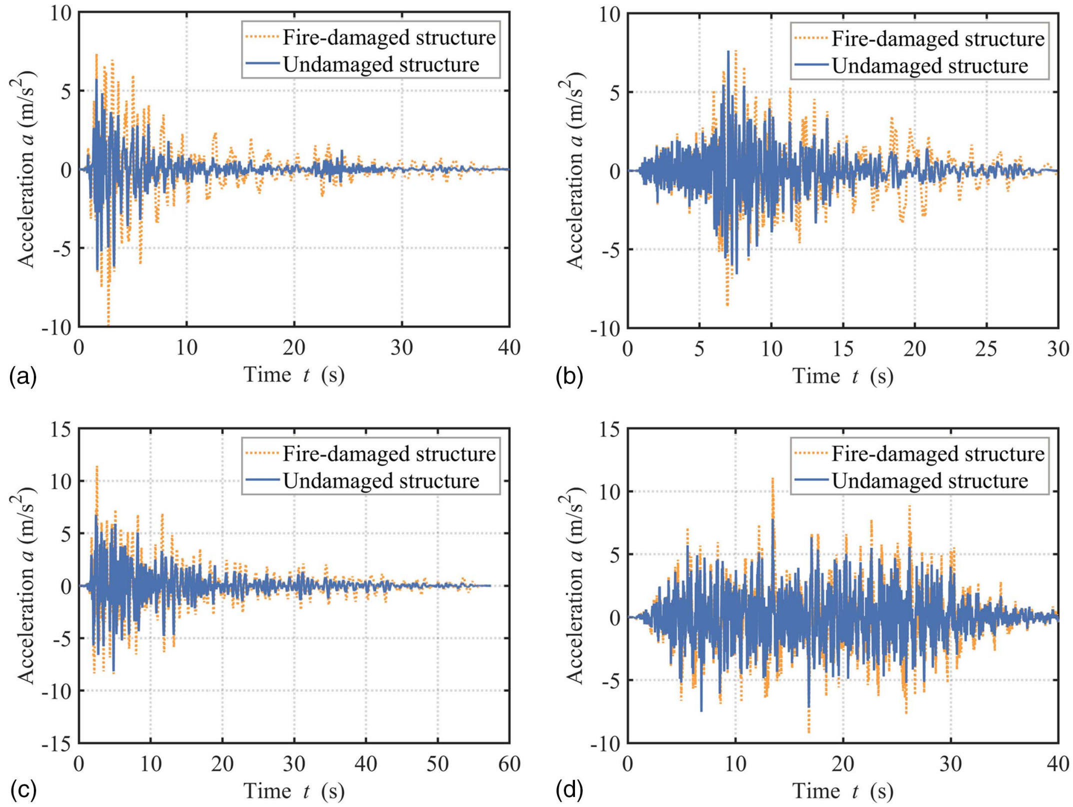


**Fig. 28.** Time histories of the structural acceleration under varying ground motions: (a) Ground motion 1; (b) Ground motion 2; (c) Ground motion 3; and (d) Ground motion 4.

**Table 11.** RMS mitigation ratios $\gamma_a$ and attenuation rates $\beta_a$ of structural acceleration responses

| Indicator | GM No. | $t_{f1}$ | $t_{f2}$ | $t_{f3}$ | $t_{f4}$ |
|---|---|---|---|---|---|
| $\gamma_a = \dfrac{\sigma_a(t_f, O)}{\sigma_{a0}}$ | GM 1 | 0.496 | 0.602 | 0.811 | 0.901 |
| | GM 2 | 0.647 | 0.707 | 0.849 | 0.930 |
| | GM 3 | 0.619 | 0.687 | 0.833 | 0.881 |
| | GM 4 | 0.670 | 0.715 | 0.844 | 0.909 |
| $\beta_a = \dfrac{\gamma_{a0} - \gamma_a}{\gamma_{a0}}$ (%) | GM 1 | 0.0 | −21.3 | −63.4 | −81.5 |
| | GM 2 | 0.0 | −9.4 | −31.3 | −43.9 |
| | GM 3 | 0.0 | −11.1 | −34.7 | −42.5 |
| | GM 4 | 0.0 | −6.7 | −25.9 | −35.7 |
| Average of $\beta_a$ (%) | — | 0.0 | −12.1 | −38.8 | −50.9 |

**Table 12.** Peak mitigation ratios $\gamma_{Pa}$ and attenuation rates $\beta_{Pa}$ of structural acceleration responses

| Indicator | GM No. | $t_{f1}$ | $t_{f2}$ | $t_{f3}$ | $t_{f4}$ |
|---|---|---|---|---|---|
| $\gamma_{Pa} = \dfrac{P_a(t_f, O)}{P_{a0}}$ | GM 1 | 0.579 | 0.663 | 0.868 | 0.898 |
| | GM 2 | 0.892 | 0.850 | 0.982 | 1.009 |
| | GM 3 | 0.631 | 0.658 | 0.794 | 0.884 |
| | GM 4 | 0.660 | 0.719 | 0.876 | 0.937 |
| $\beta_{Pa} = \dfrac{\gamma_{Pa0} - \gamma_{Pa}}{\gamma_{Pa0}}$ (%) | GM 1 | 0.0 | −14.6 | −50.0 | −55.1 |
| | GM 2 | 0.0 | 4.6 | −10.1 | −13.1 |
| | GM 3 | 0.0 | −4.2 | −25.7 | −40.0 |
| | GM 4 | 0.0 | −8.8 | −32.6 | −41.8 |
| Average of $\beta_{Pa}$ (%) | — | 0.0 | −5.7 | −29.6 | −37.5 |

Note: $P_a$ and $P_{a0}$ = peak accelerations of fire-damaged and undamaged damped structures, respectively; and $\gamma_{Pa0}$ = mitigation ratio of the peak acceleration of the undamaged damped structure.

can be obtained as given in Tables 11 and 12, respectively. It can be observed that the structural vibration control effects on both RMS and peak accelerations can degrade significantly due to the fire damage. For the case of $t_f = t_{f4}$, the residual performance in terms of the control effects on RMS and peak accelerations are reduced by 50.9% and 37.5%, respectively.

### Time Histories of Normalized Energy

In this subsection, time histories of the normalized energy for $O = 0.02$ and Ground motion 1 with different fire exposure durations $t_f$ are shown in Fig. 29. In each subgraph, the total seismic energy is divided by the energy dissipated by MYD, structural elastoplasticity, structural inherent damping, and strain or kinetic energy. It can be seen that for the undamaged case ($t_f = t_{f1} = 0$), most of the input seismic energy can be dissipated by MYD, which verifies the effectiveness of MYD and the correctness of the design method for MYD employed in this work. With the fire exposure time $t_f$ increasing, the energy dissipated by MYD decreases whereas the energy dissipated by the structural inherent damping increases because severe fire-induced damage appears in MYD. In addition, the energy dissipated by structural elastoplasticity also increases significantly because the primary structure has transformed from the elastic phase to the elastoplastic phase due to fire damage. Moreover, at the end of each subgraph, the strain or kinetic energy vanished because the structure stops vibrating at that time.

## Conclusions

Technologies for structural vibration control have received considerable attention in the last decades, but the postfire seismic

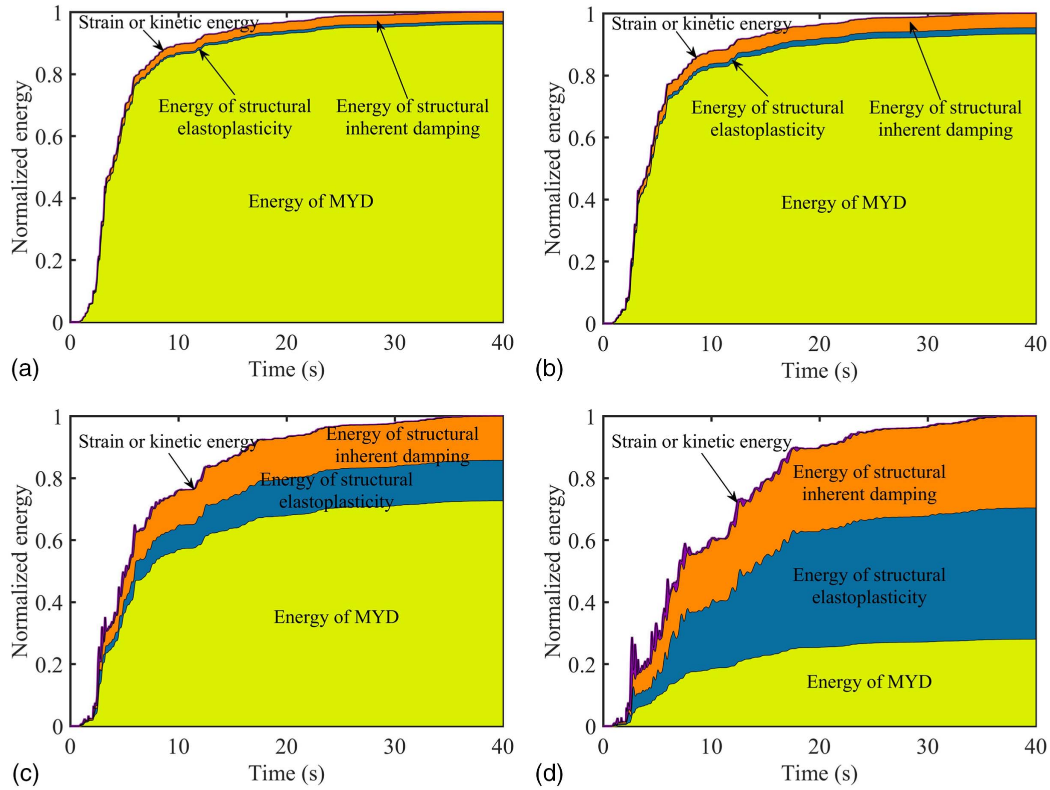


**Fig. 29.** Time histories of the normalized energy for $O = 0.02$ and Ground motion 1 with different fire exposure durations: (a) $t_f = t_{f1}$; (b) $t_f = t_{f2}$; (c) $t_f = t_{f3}$; and (d) $t_f = t_{f4}$.

performance of those damped structures is still unclear. This is the first work to investigate the residual performance of a fire-damaged SDOF concrete structure with MYDs, and authors admit that this is a relatively challenging work because it requires a comprehensive understanding of both the fields of structural vibration mitigation and structural fire safety.

One major contribution of the current work is the establishment of the methodology for investigating the residual seismic performance of the fire-damaged concrete structures with MYDs, where a 1-story RC frame structure with four carefully designed MYDs are employed as the research object in the case study. Moreover, this work is also the meaningful guidance for designing general damped structures (such as the steel structure with buckling restrained braces) considering both the fire and earthquake effects simultaneously.

In terms of the proposed methodology, the natural fire curves are determined based on the specified fire compartment, and then 16 fire scenarios are adopted considering different fire exposure duration and opening factors. Thereon, the temperature profiles of structural components and MYDs can be determined by Kodur's model and Abaqus software, respectively. On top of that, the residual performance of the damped structure can be studied at the material level. Specifically, the residual strength and elastic modulus of steel bars and MYDs are computed from the fitting formulas based on the data in Eurocode, and the damage of the concrete can be accounted for by the 500°C isotherm method. Thereon, the residual performance of the primary structure and MYDs in the structural level can be obtained from OpenSEES and Abaqus software, respectively. In addition, the Bouc-Wen and bilinear models are used to represent the hysteretic characteristics of the primary structure and MYDs, respectively. Finally, the stochastic structural responses can be obtained from the equivalent linearization and pseudoexcitation methods.

As another main contribution of this work, the residual performance can be derived quantitatively with the proposed indicators, and it is verified that the seismic performance of the SDOF concrete structure with MYDs can be reduced significantly by fire damage. Specifically, the performance indicators of the displacement and acceleration ratios, and energy filtering ratio together with their attenuation rates are defined firstly. Then, it can be observed that the seismic performance of the damped structure can be reduced by 180.7% in the worst scenario, and this performance reduction can also be seen from the PSDFs. Furthermore, four recorded ground motions are employed to conduct the time-domain analyses, and the degradation of seismic performance of the damped structure due to a fire is once again verified from the results of displacement, acceleration, and energy time histories.

Based on the aforementioned two major contributions of the proposed methodology and performance indicators, necessary retrofitting strategies could be presented to repair the existing fire-damaged damped structures and to avoid unreasonable demolition work. Furthermore, combining the proposed performance indicators with the reliability analysis, structural safety can be better ensured by designing damped structures with redundancy. In such a way, property losses and casualties might be avoided.

For future perspectives, numerical analyses for multiple-degree-of-freedom (MDOF) damped structures incorporating the spatial distribution of the fire are of great importance. Although the authors have already finished most of the analyses for the MDOF damped structures, they are not included in this paper. Because some considerations about the spatial quantities and nonlinear pseudoexcitation method for MDOF structures can make the



J. Struct. Eng., 2022, 148(4): 04022003

current paper excessively long, they will be published in our next few studies.

## Data Availability Statement

Some or all data, models, or codes that support the findings of this study are available from the corresponding author upon reasonable request.

## Acknowledgments

Financial support from the National Natural Science Foundation of China through Grant No. 51978525 is highly appreciated. The authors would also like to thank Professor Xiaojia Shelly Zhang of University of Illinois at Urbana-Champaign for proofreading this work.

## References

ACI (American Concrete Institute). 2007. *Code requirements for determining fire resistance of concrete and masonry construction assemblies*. Detroit: ACI.

Asai, T., Y. Araki, and K. Ikago. 2017. "Energy harvesting potential of tuned inertial mass electromagnetic transducers." *Mech. Syst. Sig. Process.* 84 (Feb): 659–672. https://doi.org/10.1016/j.ymssp.2016.07.048.

BSI (British Standard Institution). 2002. *Eurocode 1: Actions on structures–Part 1-2: General actions–Actions on structures exposed to fire*. BS EN 1991-1-2-2002. London: BSI.

BSI (British Standard Institution). 2004a. *Eurocode 2: Design of concrete structures–Part 1-1: General rules and rules for buildings*. BS EN 1992-1-1:2004. London: BSI.

BSI (British Standard Institution). 2004b. *Eurocode 2: Design of concrete structures–Part 1-2: General rules–Structural fire design*. BS EN 1992-1-2:2004. London: BSI.

BSI (British Standard Institution). 2005. *Eurocode 3: Design of steel structures–Part 1-2: General rules–Structural fire design*. BS EN 1993-1-2:2005. London: BSI.

Buchanan, A. H., and A. K. Abu. 2017. *Structural design for fire safety.* Chichester, UK: Wiley.

China Ministry of Housing and Urban-Rural Construction. 2015. *Chinese code for design of concrete structures*. GB 50010-2010. Beijing: China Architecture & Building Press.

China Ministry of Housing and Urban-Rural Construction. 2016a. *Chinese code for seismic design of buildings*. GB 50011-2010. Beijing: China Architecture & Building Press.

China Ministry of Housing and Urban-Rural Construction. 2016b. *Chinese code for thermal design of civil building*. GB 50176-2016. Beijing: China Architecture & Building Press.

Chipperfield, A. J. 1995. "The Matlab genetic algorithm toolbox." In *IEE colloquium on applied control techniques using MATLAB*, 10–10. London: Institution of Electrical Engineers.

Dassault Systemes Simulia Corporation. 2014. *Abaqus: A finite element analysis software*. Providence, RI: Simulia.

Gutierrez Soto, M., and H. Adeli. 2013. "Tuned mass dampers." *Arch. Comput. Methods Eng.* 20 (4): 419–431. https://doi.org/10.1007/s11831-013-9091-7.

Harmathy, T. Z., and M. A. Sultan. 1988. "Correlation between the severities of the ASTM E119 and ISO 834 fire exposures." *Fire Saf. J.* 13 (2): 163–168. https://doi.org/10.1016/0379-7112(88)90011-2.

Hurtado, J. E., and A. H. Barbat. 2000. "Equivalent linearization of the Bouc–Wen hysteretic model." *Eng. Struct.* 22 (9): 1121–1132. https://doi.org/10.1016/S0141-0296(99)00056-5.

Ikago, K., K. Saito, and N. Inoue. 2012. "Seismic control of single-degree-of-freedom structure using tuned viscous mass damper." *Earthquake Eng. Struct. Dyn.* 41 (3): 453–474. https://doi.org/10.1002/eqe.1138.

Jia, Y., L. Li, C. Wang, Z. Lu, and R. Zhang. 2019. "A novel shape memory alloy damping inerter for vibration mitigation." *Smart Mater. Struct.* 28 (11): 115002. https://doi.org/10.1088/1361-665X/ab3dc8.

Jia, Y., Z. Lu, L. Li, and C. Wang. 2020. "A hybrid steel–shape memory alloy prestressed concrete beam for improved fire resistance." *Struct. Control Health Monit.* 27 (10): e2601. https://doi.org/10.1002/stc.2601.

Jin, L., R. Zhang, G. Dou, and X. Du. 2018. "Fire resistance of steel fiber reinforced concrete beams after low-velocity impact loading." *Fire Saf. J.* 98 (Jun): 24–37. https://doi.org/10.1016/j.firesaf.2018.04.003.

Kelly, J. M., R. Skinner, and A. Heine. 1972. "Mechanisms of energy absorption in special devices for use in earthquake resistant structures." *Bull. N. Z. Soc. Earthquake Eng.* 5 (3): 63–88. https://doi.org/10.5459/bnzsee.5.3.63-88.

Kodur, V. K. R., B. Yu, and M. M. S. Dwaikat. 2013. "A simplified approach for predicting temperature in reinforced concrete members exposed to standard fire." *Fire Saf. J.* 56 (Feb): 39–51. https://doi.org/10.1016/j.firesaf.2012.12.004.

Li, W. S., and X. W. Deng. 2011. "The temperature field finite element analysis of concrete beam after fire based on Abaqus." *Appl. Mech. Mater.* 90–93 (Sep): 3089–3092. https://doi.org/10.4028/www.scientific.net/AMM.90-93.3089.

Lie, T. T., and E. M. A. Denham. 1993. *Factors affecting the fire resistance of circular hollow steel columns filled with bar-reinforced concrete*. NRC-CNRC Internal Rep. No. 651. Ottawa: National Research Council of Canada, Institute for Research in Construction.

Lin, J., W. Zhang, and F. W. Williams. 1994. "Pseudo-excitation algorithm for nonstationary random seismic responses." *Eng. Struct.* 16 (4): 270–276. https://doi.org/10.1016/0141-0296(94)90067-1.

Lin, J., and Y. Zhang. 2004. *Pseudo excitation method for random vibration*. Beijing: Science Press.

Lin, J. H., Y. H. Zhang, and Y. Zhao. 2011. "Pseudo excitation method and some recent developments." *Procedia Eng.* 14 (Jan): 2453–2458. https://doi.org/10.1016/j.proeng.2011.07.308.

Maraveas, C., Z. C. Fasoulakis, and K. D. Tsavdaridis. 2017a. "Mechanical properties of high and very high steel at elevated temperatures and after cooling down." *Fire Sci. Rev.* 6 (1): 1–13. https://doi.org/10.1186/s40038-017-0017-6.

Maraveas, C., Z. C. Fasoulakis, and K. D. Tsavdaridis. 2017b. "Post-fire assessment and reinstatement of steel structures." *J. Struct. Fire Eng.* 8 (2): 181–201. https://doi.org/10.1108/JSFE-03-2017-0028.

Mazza, F. 2015. "Seismic vulnerability and retrofitting by damped braces of fire-damaged R.C. framed buildings." *Eng. Struct.* 101 (Oct): 179–192. https://doi.org/10.1016/j.engstruct.2015.07.027.

Mazza, F. 2016. "Effects of near-fault vertical earthquakes on the nonlinear incremental response of R.C. base-isolated structures exposed to fire." *Bull. Earthquake Eng.* 14 (2): 433–454. https://doi.org/10.1007/s10518-015-9826-y.

Mazza, F. 2017. "Behaviour during seismic aftershocks of R.C. base-isolated framed structure with fire-induced damage." *Eng. Struct.* 140 (Jun): 458–472. https://doi.org/10.1016/j.engstruct.2017.03.008.

Mazza, F., and A. Vulcano. 2010. "Nonlinear dynamic response of R.C. framed structures subjected to near-fault ground motions." *Bull. Earthquake Eng.* 8 (6): 1331–1350. https://doi.org/10.1007/s10518-010-9180-z.

McKenna, F. 2011. "OpenSees: A framework for earthquake engineering simulation." *Comput. Sci. Eng.* 13 (4): 58–66. https://doi.org/10.1109/MCSE.2011.66.

Ni, S., and A. C. Birely. 2018. "Post-fire seismic behavior of reinforced concrete structural walls." *Eng. Struct.* 168 (Aug): 163–178. https://doi.org/10.1016/j.engstruct.2018.04.018.

Oliphant, T. E. 2007. "Python for scientific computing." *Comput. Sci. Eng.* 9 (3): 10–20. https://doi.org/10.1109/MCSE.2007.58.

Oliveira, F., M. A. Botto, P. Morais, and A. Suleman. 2018. "Semi-active structural vibration control of base-isolated buildings using magnetorheological dampers." *J. Low Freq. Noise Vibr. Act. Control* 37 (3): 565–576. https://doi.org/10.1177/1461348417725959.

Pan, C., and R. Zhang. 2018. "Design of structure with inerter system based on stochastic response mitigation ratio." *Struct. Control Health Monit.* 25 (6): e2169. https://doi.org/10.1002/stc.2169.

Quayyum, S., and T. Hassan. 2018. "Seismic performance of a fire-exposed moment-resisting frame." *J. Struct. Eng.* 144 (11): 04018206. https://doi.org/10.1061/(ASCE)ST.1943-541X.0002201.

Rofooei, F. R., A. Mobarake, and G. Ahmadi. 2001. "Generation of artificial earthquake records with a nonstationary Kanai–Tajimi model." *Eng. Struct.* 23 (7): 827–837. https://doi.org/10.1016/S0141-0296(00)00093-6.

Wen, Y.-K. 1976. "Method for random vibration of hysteretic systems." *J. Eng. Mech. Div.* 102 (2): 249–263. https://doi.org/10.1061/JMCEA3.0002106.

Witek, A., D. Gawin, F. Pesavento, and B. A. Schrefler. 2006. "Finite element analysis of various methods for protection of concrete structures against spalling during fire." *Comput. Mech.* 39 (3): 271–292. https://doi.org/10.1007/s00466-005-0024-7.

Xu, L., Y. Yu, and Y. Cui. 2018. "Active vibration control for seismic excited building structures under actuator saturation, measurement stochastic noise and quantisation." *Eng. Struct.* 156: 1–11. https://doi.org/10.1016/j.engstruct.2017.11.021.

Zhang, R., C. Wang, C. Pan, H. Shen, Q. Ge, and L. Zhang. 2018. "Simplified design of elastoplastic structures with metallic yielding dampers based on the concept of uniform damping ratio." *Eng. Struct.* 176: 734–745. https://doi.org/10.1016/j.engstruct.2018.09.009.